ATLAS CONF Note

ATLAS-CONF-2018-31

6th July 2018

Combined measurements of Higgs boson production and decay using up to 80 fb^{-1} of proton—proton collision data at $\sqrt{s}$ = 13 TeV collected with the ATLAS experiment

The ATLAS Collaboration

Combined measurements of Higgs boson production cross-sections, branching fractions and couplings are presented in the Higgs boson decay channels into $\gamma\gamma$, ZZ^*, WW^*, $\tau\tau$, $\mu\mu$ and $b\bar{b}$, using up to 79.8 fb^{-1} of proton—proton collision data at $\sqrt{s}$ = 13 TeV collected with the ATLAS experiment. Results are presented for the gluon-gluon fusion and vector-boson fusion processes, and associated production with vector bosons or top quarks. The combined measurement yields an observed (expected) significance for the vector-boson fusion production process of 6.5σ (5.3σ). This single-experiment observation follows an earlier observation in the combination of ATLAS and CMS measurements. The results are interpreted in terms of modifiers applied to the Standard Model couplings of the Higgs boson to other particles, and are used to set exclusion limits on new phenomena. No significant deviations from Standard Model predictions are observed.

ATLAS-CONF-2018-031
06 July 2018

1 Introduction

Following the discovery of the Higgs boson H by the ATLAS [1] and CMS [2] experiments, its properties have been probed using proton–proton (pp) collision data produced by the Large Hadron Collider (LHC) at CERN. The coupling properties of the Higgs boson to other Standard Model (SM) particles, such as its production cross-sections in pp collisions and decay branching ratios can be precisely computed within the SM. Measurements of these properties can provide stringent tests of its validity.

Higgs boson production and decay rates have been precisely determined using the Run 1 dataset, through the combination of ATLAS and CMS measurements [3]. More recently, these measurements have been extended using the Run 2 dataset recorded by the ATLAS detector during 2015, 2016 and 2017, using up to 79.8 fb^{-1} of proton–proton collision data in analyses targeting the $H\to\gamma\gamma$ [4], $H\to ZZ^*\to 4\ell$[1] [5], $H\to WW^*$ [6], $H\to\tau\tau$ [7], $H\to b\bar{b}$ [8] and $H\to\mu\mu$ [9] decay chanels, as well as two analyses targeting associated production with a top–antitop pair [10–12]. This note presents measurements of Higgs properties at $\sqrt{s}$ = 13 TeV obtained in the combination of these results, using a methodology similar to that of Ref. [3]. A Higgs boson mass value of m_H = 125.09 GeV, corresponding to the central value of the combination of ATLAS and CMS measurements in Run 1 [13], is used for SM predictions. Similar measurements have also been reported by the CMS collaboration [14–21].

The note is structured as follows: Section 2 describes the data and simulation samples and Section 3 overviews the measurements in individual decay channels which are used as inputs to the combination. Section 4 provides a short description of the statistical procedures. The measurement of the signal strength μ, defined as the ratio of the total Higgs boson signal yield to its SM prediction, is presented in Section 5.1. Measurements of the cross-sections of the main production processes, assuming SM predictions for the branching ratios, are then shown in Section 5.2. The production modes considered are gluon-gluon fusion (ggF), weak vector-boson fusion (VBF), associated production with a weak vector boson $V = W$ or Z (VH), and associated production with a top–antitop pair ($t\bar{t}H$) or with a single top quark (tH). Section 5.3 presents a parameterization where the measured quantities are the cross-section times branching ratio of the process $gg\to H\to ZZ^*$, the cross-section ratios $\sigma_i/\sigma_{\text{ggF}}$ for all considered production modes except ggF, and the ratios of branching fractions B_f/B_{ZZ} for all considered decay modes except $H\to ZZ^*$. Common systematic uncertainties and modeling assumptions partially cancel in these ratios, reducing the model dependence. Potential deviations from SM predictions are then probed in a framework of multiplicative modifiers κ applied to the SM values of Higgs boson couplings [22], presented in Section 5.4. Finally, Section 5.5 presents an interpretation of the data within two benchmark models of beyond the SM (BSM) phenomena. Indirect limits on model parameters are set following a methodology similar to that of Ref. [23]. Section 6 summarizes the results.

2 Data and simulated samples

The results of this note are based on proton–proton collision data collected by the ATLAS experiment [24, 25] in 2015, 2016 and 2017, with the LHC operating at a centre-of-mass energy of 13 TeV. The integrated luminosities of the datasets used in each input analysis are shown in Table 1. The analyses are described in Section 3.

[1] ℓ denotes the light leptons e and μ.

Table 1: Integrated luminosity of the dataset used for each input analysis to the combination.

Analysis	Integrated luminosity (fb^{-1})
$H \to \gamma\gamma$ (including $t\bar{t}H$, $H \to \gamma\gamma$)	79.8
$H \to ZZ^* \to 4\ell$ (including $t\bar{t}H$, $H \to ZZ^* \to 4\ell$)	79.8
$H \to WW^* \to e\nu\mu\nu$	36.1
$H \to \tau\tau$	36.1
VH, $H \to b\bar{b}$	36.1
$H \to \mu\mu$	79.8
$t\bar{t}H$, $H \to b\bar{b}$ and $t\bar{t}H$ multilepton	36.1

The simulated Higgs boson samples used to describe the signal processes are described below. Simulated background samples are described in the individual references for the input analyses. Higgs boson production via gluon-gluon fusion is simulated using the Powheg Box [26–29] NNLOPS implementation [30, 31]. The event generator uses HNNLO [32] to reweight the inclusive Higgs boson rapidity distribution produced by the next-to-leading order (NLO) generation of $pp \to H$ + parton, with the scale of each parton emission determined using the MiNLO procedure [33]. The PDF4LHC15 parton distribution functions (PDFs) are used for the central prediction and uncertainty. The sample is normalised such that it reproduces the total cross-section predicted by a next-to-next-to-next-to-leading-order (N^3LO) QCD calculation with NLO electroweak corrections applied [34–38]. The NNLOPS generator reproduces the Higgs boson p_{T} distribution predicted by the NNLO plus next-to-next-to-leading logarithm (NNLL) calculation of Hres2.3 [39], which includes the effects of top- and bottom-quark masses and uses dynamical renormalisation and factorisation scales.

The VBF and VH production processes are simulated to NLO accuracy in QCD using the Powheg Box [40] generator with the PDF4LHC15 set of PDFs. The VBF sample is normalised to an approximate-NNLO QCD cross-section with NLO electroweak corrections applied [34, 41–43]. The VH samples are normalised to cross-sections calculated at NNLO in QCD with NLO electroweak corrections [44, 45] and additional NLO QCD corrections [46] for the $gg \to ZH$ subprocess [34].

Higgs boson production in association with a top–antitop pair is simulated at NLO accuracy in QCD using the Powheg Box generator with the PDF4LHC15 set of PDFs for the $H \to \gamma\gamma$ and $H \to ZZ^* \to 4\ell$ decay processes. For other Higgs boson decays, the MadGraph5_aMC@NLO [47] generator is used with the NNPDF3.0 set of PDFs. In both cases the sample is normalised to a calculation with NLO QCD and electroweak corrections [34, 48–51].

In addition to the primary Higgs boson processes, separate samples are used to model lower-rate processes. Higgs boson production in association with a bottom–antibottom pair ($b\bar{b}H$) is simulated using MadGraph5_aMC@NLO [52] with NNPDF2.3LO PDFs and is normalised to a cross-section calculated to NNLO in QCD [34, 53–55]. The sample includes the effect of interference with the ggF production mechanism. Higgs boson production in association with a single top quark and a W boson (tHW) is produced at LO accuracy using MadGraph5_aMC@NLO. Finally, Higgs boson production in association with a single top quark in the t-channel (tHq) is generated at LO accuracy using MadGraph5_aMC@NLO with CT10 [56] PDFs. The tH samples are normalised to NLO QCD calculations [34, 57].

The parton-level events are input to Pythia8 [58] or Herwig++ [59] to model the Higgs boson decay,

parton showering, hadronization, and multiple parton interactions (MPI). The generators are interfaced to Pythia8 for all samples except tHW. For Pythia8 the AZNLO and A14 parameter sets [60] are used, and for Herwig++ the UEEE5 parameter set is used. The particle-level Higgs boson events are passed through a Geant 4 [61, 62] simulation of the ATLAS detector [63] and reconstructed using the same analysis software as used for the data. Event pileup is included in the simulation by adding inelastic proton–proton collisions, such that the average number of interactions per bunch crossing reproduces that observed in the data. The inelastic proton–proton collisions are produced using Pythia8.

3 Individual channel measurements

Brief descriptions of the input analyses to the combination are given below. More details can be found in the individual analysis references listed in each section. The categorization is summarized in Table 2.

3.1 $H \to \gamma\gamma$

The $H \to \gamma\gamma$ analysis [4] requires the presence of two isolated photons [64] within the pseudorapidity range $|\eta| < 2.37$, excluding the region $1.37 < |\eta| < 1.52$ corresponding to the transition between the barrel and endcap sections of the electromagnetic calorimeter. The transverse momenta of the leading and subleading photons are required to be greater than $0.35 m_{\gamma\gamma}$ and $0.25 m_{\gamma\gamma}$ respectively, where $m_{\gamma\gamma}$ is the invariant mass of the diphoton system. The distribution of $m_{\gamma\gamma}$ is used to separate the Higgs boson signal from background processes. These mainly arise from $\gamma\gamma$ production, single-photon production where an additional jet in the event is misidentified as a photon, and processes where two jets are misidentified as photons.

Selected events are separated into 29 mutually exclusive categories based on the kinematics of the diphoton system and associated particles. Seven categories are defined to select $t\bar{t}H$ production [12], targeting both leptonic and hadronic top decay processes through various selections on the numbers of leptons [65, 66], jets [67], and jets tagged as containing b-quarks [68] in the event. Jets are reconstructed using the anti-k_t algorithm with a radius parameter of 0.4. Five categories are defined to select $(W \to \ell\nu)H$, $(Z \to \ell\ell)H$ and $(Z \to \nu\nu)H$ production with leptonic decays of the W or Z, based on the presence of leptons and missing transverse momentum $E_{\mathrm{T}}^{\mathrm{miss}}$ [69]. Seven categories target associated production with jets from VBF and VH processes: one category requires the presence of two jets, with the leading jet transverse momentum above 200 GeV; two select hadronic vector boson decays by requiring two jets with an invariant mass compatible with the W or Z boson mass; and four categories target VBF production by requiring forward jets in a VBF-like topology. The remaining events are classified into 10 categories according to the jet multiplicity (0, 1 or ≥ 2) and the transverse momentum of the diphoton system $p_{\mathrm{T}}^{\gamma\gamma}$.

3.2 $H \to ZZ^* \to 4\ell$

The $H \to ZZ^* \to 4\ell$ analysis [5] measures Higgs boson production cross-sections for different production modes using final states with at least two same-flavor and opposite-charge light-lepton pairs in several mutually exclusive regions of the production phase space. The largest background is continuum $(Z^{(*)}/\gamma^*)(Z^{(*)}/\gamma^*)$ production, modeled using Monte Carlo simulation. Other background contributions arise from Z + jets and $t\bar{t}$ production with two prompt leptons and are estimated using data. Boosted

decision trees are employed to separate the signal from the background processes and to enhance the sensitivity to the various Higgs boson production modes.

To distinguish the $t\bar{t}H$, VH, VBF, and ggF production modes and to enhance the purity of each kinematic selections, 11 reconstructed event categories are defined based on the presence of jets and additional leptons in the final state. Candidate events with at least one b-tagged jet and either four or more additional jets, or one additional lepton and at least two additional jets are classified in two $t\bar{t}H$-enriched categories [12]. Events failing these requirements but containing at least one additional lepton are classified in a VH-enriched category with leptonic vector boson decays. The remaining events are classified according to their jet multiplicity (0-jet, 1-jet, and $\geq$ 2-jet). Events with at least two jets are divided into two VBF-enriched categories and a region enriched in the VH production mode with a hadronically decaying vector boson using the dijet invariant mass. The selected 0-jet and 1-jet events are separated into 5 categories according to the transverse momentum of the four-lepton system.

3.3 $H \to WW^* \to e\nu\mu\nu$

The $H \to WW^* \to e\nu\mu\nu$ analysis [6] targets the ggF and VBF production modes. Signal candidates are selected by requiring the presence of an isolated $e^{\pm}\mu^{\mp}$ pair, with transverse momentum thresholds at 22 and 15 GeV for the leading and subleading lepton. Events with jets tagged as containing b-quarks are rejected to suppress background contributions originating from top-quark production. Contributions from $W \to \tau\nu$ decays in which the tau leptons subsequently decay to electrons or muons are also included.

The primary background processes are WW, top-quark, W+jets, Drell–Yan, and other diboson (WZ, $W\gamma$, $W\gamma^*$, and ZZ) production. Most of these contributions are estimated using data in kinematic regions enriched in the given process.

Selected events are classified according to the number of associated jets (N_{jets}). Exclusive $N_{\text{jets}} = 0$ and $N_{\text{jets}} = 1$ selections are enriched in signal events produced via ggF. To isolate regions with higher sensitivity, they are each further split into eight categories apiece, based on the flavour of the leading lepton (e or μ), two bins of the invariant mass of the dilepton system $m_{\ell\ell}$ and two bins of the the transverse momentum of the sub-leading lepton $p_{\text{T}}^{\ell_2}$. The distribution of the transverse mass of the dilepton plus $E_{\text{T}}^{\text{miss}}$ system is used to separate the Higgs boson signal from background in each category. The $N_{\text{jets}} \geq 2$ category is naturally sensitive to the VBF process. A central-jet veto is applied to suppress the QCD multijet background and the contribution from ggF production. The output of a boosted decision tree exploiting the kinematic properties of the two leading jets and the two leptons is used to separate the VBF Higgs boson production from background processes, including Higgs boson production via ggF.

3.4 $H \to \tau\tau$ and $H \to \mu\mu$

The $H \to \tau\tau$ analysis [7] measures the Higgs boson production cross-section in the VBF production process or in ggF production with large Higgs boson transverse momentum p_{T}^{H}. Final states with both leptonic (τ_{lep}) and hadronic (τ_{had}) decays of the tau lepton are considered. Selected lepton candidates are required to be of opposite charge, pass identification and isolation criteria and satisfy the p_{T} thresholds of the triggers used. Three mutually exclusive analysis channels, $\tau_{\text{lep}}\tau_{\text{lep}}$, $\tau_{\text{lep}}\tau_{\text{had}}$, and $\tau_{\text{had}}\tau_{\text{had}}$, are defined according to the number of selected electron, muon and hadronic tau candidates. All channels require the presence of at least one jet with high transverse momentum.

To exploit signal-sensitive event topologies, candidate events are divided into three categories targeting the VBF process and two categories targeting boosted Higgs production. The VBF categories collect events with two jets with a large pseudorapidity separation and a high invariant mass (m_{jj}). The Higgs boson decay products are required to be in the central rapidity region. One VBF category is defined by requiring the transverse momentum of the $\tau\tau$ system $p_{\mathrm{T}}^{\tau\tau}$ to be above 140 GeV, for $\tau_{\mathrm{had}}\tau_{\mathrm{had}}$ events only. The two remaining VBF categories are defined for lower and higher values of m_{jj}, with definitions that differ between the $\tau_{\mathrm{lep}}\tau_{\mathrm{lep}}$, $\tau_{\mathrm{lep}}\tau_{\mathrm{had}}$, and $\tau_{\mathrm{had}}\tau_{\mathrm{had}}$ channels. The boosted categories target signal events with large p_{T}^{H}, with contributions mainly from the ggF process. Events failing the VBF selection and with $p_{\mathrm{T}}^{\tau\tau} > 100$ GeV are selected. In order to improve the sensitivity of the analysis, two categories are defined respectively for $p_{\mathrm{T}}^{\tau\tau} > 140$ GeV and $p_{\mathrm{T}}^{\tau\tau} \leq 140$ GeV, with additional selections on the angular separation between the tau leptons. The invariant mass of the di-tau system is used as the discriminating variable. The distribution of the invariant mass of the $\tau\tau$ system is used to separate the Higgs boson signal from background. In all three sub-channels, the most important backgrounds are irreducible $Z\to\tau\tau$ events, and events with one or two jets misidentified as tau lepton decay products, primarily from multijet and W+jets production.

The $H\to\mu\mu$ search [9] uses a similar technique as $H\to\gamma\gamma$, requiring a pair of opposite-charge muons and using the distribution of the invariant mass $m_{\mu\mu}$ to separate signal from background. Events are classified into eight categories. The output of a boosted decision tree exploiting the kinematic properties of the two leading jets and the two muons is used to define two categories targeting the VBF process. In order to enhance the sensitivity of the analysis, the remaining ones are classified into three ranges of the transverse momentum $p_{\mathrm{T}}^{\mu\mu}$ of the dimuon system ($p_{\mathrm{T}}^{\mu\mu} < 15$ GeV, 15 GeV $\leq p_{\mathrm{T}}^{\mu\mu} < 50$ GeV and $p_{\mathrm{T}}^{\mu\mu} \geq 50$ GeV) and two ranges of the muon pseudorapidities η^{μ} (both muons within $|\eta^{\mu}| \leq 1$, or at least one muon outside this range), for a total of six categories. The analysis has limited sensitivity and is only included in the measurement presented in Section 5.4.3.

3.5 $VH, H\to b\bar{b}$

The search for $H\to b\bar{b}$ in the VH production mode [8] considers final states containing at least two jets of which exactly two must be tagged as containing b-hadrons. Either zero, one or two charged leptons are also required, exploring the associated production of a Higgs boson with a W or Z boson decaying leptonically as $W\to\ell\nu$, $Z\to\ell\ell$, or $Z\to\nu\nu$. Contributions from $W\to\tau\nu$ and $Z\to\tau\tau$ decays in which the tau-leptons subsequently decay to electrons or muons are also included. The most significant background contributions arise from V+heavy-flavour-jets and $t\bar{t}$ production. The normalizations of these processes are estimated using data. Other significant background sources are single-top-quark and diboson (WZ and ZZ) production. Their normalizations are obtained from theory predictions. Multijet events enter the selection due to jets mis-measured in the calorimeters and are estimated using control samples.

To enhance the signal sensitivity, selected candidate events are classified according to the charged lepton multiplicity, the vector boson transverse momentum p_{T}^{V}, and the jet multiplicity. For final states with zero or one lepton, $p_{\mathrm{T}}^{V} > 150$ GeV is required. In two-lepton final states two regions are considered, 75 GeV $< p_{\mathrm{T}}^{V} < 150$ GeV and $p_{\mathrm{T}}^{V} > 150$ GeV. Each of these regions is finally separated into a category with exactly two reconstructed jets and another with three or more. In the zero- and one-lepton channel, events with four or more jets are rejected. Topological and kinematic selection criteria are applied within each of the resulting categories. The categories providing most of the sensitivity are those requiring large p_{T}^{V}. The categories with low sensitivity are important to constrain the contributions of the dominant background processes. Multivariate discriminants making use of boosted decision trees, incorporating the

event kinematics and topology in addition to the dijet invariant mass, are employed in each lepton channel and analysis region to separate the signal process from the sum of the expected background processes.

3.6 $t\bar{t}H$, $H \to b\bar{b}$ and $t\bar{t}H$ multilepton analyses

Searches for the associated production of the Higgs boson with a top–antitop pair have been performed using Higgs boson decays to $b\bar{b}$ [10] and in in multilepton final states, targeting Higgs boson decays to WW^*, ZZ^* and $\tau\tau$ [11, 12]. These analyses complement the selections sensitive to $t\bar{t}H$ production defined in the analyses of the $H\to\gamma\gamma$ and $H\to ZZ^*\to 4\ell$ decay channels, described in Sections 3.1 and 3.2.

The search for $t\bar{t}H$ production with $H \to b\bar{b}$ employs two selections, optimised for single-lepton and dilepton final states of $t\bar{t}$ decays. In the single lepton channel, events are required to have one isolated electron or muon and at least five jets, of which at least two must be identified as containing b-hadrons. In the dilepton channel, events are required to have two opposite-charge leptons and at least three jets, of which at least two must be identified as containing b-hadrons. Candidate events are classified into eleven (seven) orthogonal categories in the single lepton (dilepton) channel, according to the jet multiplicity and the values of the b-tagging discriminant for the jets. In the single-lepton channel, an additional category, referred to as *boosted*, is designed to select events with large transverse momenta for the Higgs candidate ($p_{\mathrm{T}}^{H} > 200$ GeV) and one of the top quark candidates ($p_{\mathrm{T}}^{t} > 250$ GeV). In each signal-enriched region, a boosted decision tree exploiting kinematic information of the events is employed to separate $t\bar{t}H$ production from background processes. Some of the selected regions are enriched in the main background processes, $t\bar{t}$ + light flavour, $t\bar{t}+ \geq 1b$, $t\bar{t}+ \geq 1c$, $t\bar{t}+V$ and non-$t\bar{t}$ production, and are used to estimate their yields.

The $t\bar{t}H$ search with Higgs boson decays to WW^*, ZZ^* and $\tau\tau$ exploits several multilepton signatures resulting from leptonic decays of vector bosons and/or the presence of hadronically-decaying τ lepton candidates. Seven final states, categorised by the number and flavour of reconstructed charged lepton candidates, are examined. They are: one lepton with two hadronic τ candidates, two same-charge leptons with zero or one hadronic τ candidates, two opposite-charge leptons with one hadronic τ candidate, three leptons with zero or one hadronic τ candidates, and four leptons. Events in all channels are required to have at least two jets, at least one of which must be b-tagged. Additional requirements are employed for each final state. The largest backgrounds are fake and non-prompt leptons, primarily arising from semileptonic b-hadron decays in $t\bar{t}$ events, electron charge misreconstruction in events where opposite-sign leptons are produced and the production of $t\bar{t}+W/Z$. Multivariate analysis techniques exploiting the kinematic properties and topologies of the selected events have been applied in most channels to improve the discrimination between the signal and the background. The number of expected background events and the associated kinematic distributions are estimated using data-driven methods and simulation.

Table 2: Summary of the signal regions entering the combined measurements. Each 0-jet and 1-jet $H \to WW^*$ entry corresponds to two categories for a leading lepton flavour of either e or μ. For $H \to \tau\tau$, each entry corresponds to 3 categories for $\tau_{\text{lep}}\tau_{\text{lep}}$, $\tau_{\text{lep}}\tau_{\text{had}}$ and $\tau_{\text{had}}\tau_{\text{had}}$, unless otherwise specified. "Multilepton" refers to decays of the Higgs boson with one or more leptons, and encompasses $H \to WW^*$, $H \to \tau\tau$, and $H \to ZZ^*$ excluding $H \to ZZ^* \to 4\ell$. The $H \to \mu\mu$ analysis only enters in the measurement in Section 5.4.3 and is not included here.

$H \to \gamma\gamma$	$H \to ZZ^* \to 4\ell$	$H \to WW^*$	$H \to \tau\tau$	$H \to b\bar{b}$
$t\bar{t}H$ leptonic (3 categories) $t\bar{t}H$ hadronic (4 categories)	$t\bar{t}H$ leptonic $t\bar{t}H$ hadronic	$t\bar{t}H$ multilepton 1 ℓ + 2 τ_{had} $t\bar{t}H$ multilepton 2 opposite-sign ℓ $t\bar{t}H$ multilepton 2 same-sign ℓ (categories for 0 or 1 τ_{had}) $t\bar{t}H$ multilepton 3 ℓ (categories for 0 or 1 τ_{had}) $t\bar{t}H$ multilepton 4 ℓ		$t\bar{t}H$ 1 ℓ, boosted $t\bar{t}H$ 1 ℓ, resolved (11 categories) $t\bar{t}H$ 2 ℓ (7 categories)
VH 2 ℓ VH 1 ℓ, $p_{\text{T}}^{\ell+E_{\text{T}}^{\text{miss}}} \geq 150$ GeV VH 1 ℓ, $p_{\text{T}}^{\ell+E_{\text{T}}^{\text{miss}}} <150$ GeV VH $E_{\text{T}}^{\text{miss}}$, $E_{\text{T}}^{\text{miss}} \geq 150$ GeV VH $E_{\text{T}}^{\text{miss}}$, $E_{\text{T}}^{\text{miss}} <150$ GeV VH+VBF $p_{\text{T}}^{j1} \geq 200$ GeV VH hadronic (2 categories)	VH leptonic 0-jet, $p_{\text{T}}^{4\ell} \geq 100$ GeV 2-jet, $m_{jj} < 120$ GeV			2 ℓ, $75 \leq p_{\text{T}}^{V} < 150$ GeV, $N_{\text{jets}} = 2$ 2 ℓ, $75 \leq p_{\text{T}}^{V} < 150$ GeV, $N_{\text{jets}} \geq 3$ 2 ℓ, $p_{\text{T}}^{V} \geq 150$ GeV, $N_{\text{jets}} = 2$ 2 ℓ, $p_{\text{T}}^{V} \geq 150$ GeV, $N_{\text{jets}} \geq 3$ 1 ℓ $p_{\text{T}}^{V} \geq 150$ GeV, $N_{\text{jets}} = 2$ 1 ℓ $p_{\text{T}}^{V} \geq 150$ GeV, $N_{\text{jets}} = 3$ 0 ℓ, $p_{\text{T}}^{V} \geq 150$ GeV, $N_{\text{jets}} = 2$ 0 ℓ, $p_{\text{T}}^{V} \geq 150$ GeV, $N_{\text{jets}} = 3$
VBF, $p_{\text{T}}^{\gamma\gamma jj} \geq 25$ GeV (2 categories) VBF, $p_{\text{T}}^{\gamma\gamma jj} <25$ GeV (2 categories)	2-jet VBF, $p_{\text{T}}^{j1} \geq 200$ GeV 2-jet VBF, $p_{\text{T}}^{j1} <200$ GeV	2-jet VBF	VBF $p_{\text{T}}^{\tau\tau} > 140$ GeV ($\tau_{\text{had}}\tau_{\text{had}}$ only) VBF high-m_{jj} VBF low-m_{jj}	
2-jet, $p_{\text{T}}^{\gamma\gamma} \geq 200$ GeV 2-jet, 120 GeV$\leq p_{\text{T}}^{\gamma\gamma} <200$ GeV 2-jet, 60 GeV$\leq p_{\text{T}}^{\gamma\gamma} <120$ GeV 2-jet, $p_{\text{T}}^{\gamma\gamma} < 60$ GeV 1-jet, $p_{\text{T}}^{\gamma\gamma} \geq 200$ GeV 1-jet, 120 GeV$\leq p_{\text{T}}^{\gamma\gamma} <200$ GeV 1-jet, 60 GeV$\leq p_{\text{T}}^{\gamma\gamma} <120$ GeV 1-jet, $p_{\text{T}}^{\gamma\gamma} < 60$ GeV 0-jet (2 categories)	1-jet, $p_{\text{T}}^{4\ell} \geq 120$ GeV 1-jet, 60 GeV$\leq p_{\text{T}}^{4\ell} <120$ GeV 1-jet, $p_{\text{T}}^{4\ell} < 60$ GeV 0-jet, $p_{\text{T}}^{4\ell} < 100$ GeV	1-jet, $m_{\ell\ell} < 30$ GeV, $p_{\text{T}}^{\ell_2} < 20$ GeV 1-jet, $m_{\ell\ell} < 30$ GeV, $p_{\text{T}}^{\ell_2} \geq 20$ GeV 1-jet, $m_{\ell\ell} \geq 30$ GeV, $p_{\text{T}}^{\ell_2} < 20$ GeV 1-jet, $m_{\ell\ell} \geq 30$ GeV, $p_{\text{T}}^{\ell_2} \geq 20$ GeV 0-jet, $m_{\ell\ell} < 30$ GeV, $p_{\text{T}}^{\ell_2} < 20$ GeV 0-jet, $m_{\ell\ell} < 30$ GeV, $p_{\text{T}}^{\ell_2} \geq 20$ GeV 0-jet, $m_{\ell\ell} \geq 30$ GeV, $p_{\text{T}}^{\ell_2} < 20$ GeV 0-jet, $m_{\ell\ell} \geq 30$ GeV, $p_{\text{T}}^{\ell_2} \geq 20$ GeV	Boosted, $p_{\text{T}}^{\tau\tau} > 140$ GeV Boosted, $p_{\text{T}}^{\tau\tau} \leq 140$ GeV	

4 Statistical model

The statistical methods used in this note follow those of Ref. [3]. The results of the combination are obtained from a likelihood function defined as the product of the likelihoods of each input analysis. These are themselves products of likelihoods computed in mutually exclusive regions selected in the analysis, referred to as analysis categories.

The number of signal events in each analysis category k is expressed as

$$n_k^{\text{signal}} = \mathcal{L}_k \sum_i \sum_f (\sigma \times \text{B})_{if} (\epsilon \times A)_k^{if} \tag{1}$$

where the sum runs over production phase space regions i and decay final states f, $\mathcal{L}_k$ is the integrated luminosity of the dataset used in category k, and $(\epsilon \times A)_k^{if}$ is the acceptance times efficiency factor in category k for production region i and final state f. The $(\sigma \times \text{B})_{if}$ for each relevant pair (i, f) are the parameters of interest of the model. They are expressed in terms of smaller sets of parameters to perform the measurements presented in this paper: in terms of a single signal strength parameter μ (Section 5.1), of the cross-sections σ_i in each of the main production modes (Section 5.2), of ratios of cross-sections and branching ratios (Section 5.3) or of coupling modifiers (Section 5.4). Additional parameters, denoted as nuisance parameters, are used to describe systematic uncertainties and background quantities that are constrained by sidebands or control regions in data.

The measurement of the parameters of interest is carried out using a statistical test based on the profile likelihood ratio [70],

$$\Lambda(\boldsymbol{\alpha}) = \frac{L(\boldsymbol{\alpha}, \hat{\hat{\boldsymbol{\theta}}}(\boldsymbol{\alpha}))}{L(\hat{\boldsymbol{\alpha}}, \hat{\boldsymbol{\theta}})} , \tag{2}$$

where $\boldsymbol{\alpha}$ and $\boldsymbol{\theta}$ are respectively the parameters of interest and the nuisance parameters. In the numerator, the nuisance parameters are set to their *profiled* values $\hat{\hat{\boldsymbol{\theta}}}(\boldsymbol{\alpha})$, which maximize the likelihood function for fixed values of the parameters of interest $\boldsymbol{\alpha}$. In the denominator, both the parameters of interest and the nuisance parameters are set to the values $\hat{\boldsymbol{\alpha}}$ and $\hat{\boldsymbol{\theta}}$ respectively which jointly maximize the likelihood.

In the asymptotic regime, in which the likelihood is approximately Gaussian, the value of $-2 \log \Lambda(\boldsymbol{\alpha})$ follows a χ^2 distribution with a number of degrees of freedom n equal to the dimensionality of the vector $\boldsymbol{\alpha}$ [70]. This property is assumed to hold for all the results presented in the following sections. Confidence intervals for a confidence level (CL) $1 - p$ are then defined as the regions with values of $-2 \log \Lambda(\boldsymbol{\alpha})$ below a threshold $F^{-1}_{\chi^2_n}(1 - p)$, where $F_{\chi^2_n}$ is the cumulative distribution function of the χ^2 with n degrees of freedom.

Uncertainties are in some cases broken down into components for theoretical uncertainties affecting the background processes, theoretical uncertainties affecting the Higgs boson signal, experimental uncertainties and statistical uncertainties. The uncertainties for each component are derived by fixing the associated nuisance parameters to their best-fit values $\hat{\theta}$ in both the numerator and denominator of Λ, for each component in turn following the order in which they are listed above. The resulting uncertainty at each step is then subtracted in quadrature from the uncertainty obtained in the previous step (in the first step, from the total uncertainty) to obtain the uncertainty value for each component. The statistical uncertainty component is obtained in the last step, with all nuisance parameters fixed except for the ones that are only constrained by data, such as parameters used to describe data-driven background estimations.

For the systematic uncertainties reported in the detailed breakdowns of Tables 3 and 5, a simpler procedure is used: in each case the corresponding nuisance parameters are fixed to their best fit values, while other nuisance parameters are left free, and the resulting uncertainty is subtracted in quadrature from the total uncertainty.

The compatibility with the Standard Model is quantified using the test statistic $\lambda_{\mathrm{SM}} = -2\log\Lambda(\boldsymbol{\alpha} = \boldsymbol{\alpha}_{\mathrm{SM}})$, where $\boldsymbol{\alpha}_{\mathrm{SM}}$ are the Standard Model values of the parameters of interest. A p-value[2] p_{SM} for the compatibility is computed in the asymptotic approximation as $p_{\mathrm{SM}} = 1 - F_{\chi^2_n}(\lambda_{\mathrm{SM}})$, with n equal to the number of free parameters of interest.

Expected results in the SM hypothesis are obtained using the Asimov dataset technique [70].

5 Combined measurements

5.1 Global signal strength

The global signal strength μ is determined following the procedures used for the measurements performed at $\sqrt{s} = 7$ and 8 TeV [3]. The signal yields are expressed in terms of a single parameter defined as the ratio

$$\mu = \frac{(\sigma \times \mathrm{B})_{if}}{(\sigma \times \mathrm{B})^{\mathrm{SM}}_{if}}, \tag{3}$$

of the observed yields to their SM expectations, for all production processes i and decay final states f. It corresponds to a global scaling of the expected Higgs boson yield in all categories by a single value. Its definition is dependent on the SM predictions for each production mode cross-section σ_i and decay branching ratio B_f, and the uncertainties on these predictions are included as nuisance parameters as described in Section 4.

It is measured to be

$$\mu = 1.13^{+0.09}_{-0.08} = 1.13 \pm 0.05\,(\mathrm{stat.}) \pm 0.05\,(\mathrm{exp.})\,^{+0.05}_{-0.04}\,(\mathrm{sig.\ th.}) \pm 0.03\,(\mathrm{bkg.\ th.})$$

where the total uncertainty is decomposed into components for statistical uncertainties, experimental systematic uncertainties, and theory uncertainties on signal and background modelling, following the procedure outlined in Section 4. The signal theory component includes uncertainties due to missing higher-order perturbative QCD and electroweak corrections in the MC simulation, the choice of the PDF sets, the matching between the hard-scattering process and the underlying event, the parton shower and hadronization models, and branching ratio uncertainties. The measurement is consistent with the SM prediction with a p-value of $p_{\mathrm{SM}} = 13\%$. The value of $-2\log\Lambda(\mu)$ as a function of μ is shown in Figure 1, for the full likelihood and the versions with some nuisance parameters fixed to their best-fit values to obtain the components of the uncertainty as described in Section 4.

Table 3 shows a summary of the leading uncertainties in the combined measurement of the global signal strength, with uncertainties computed as described in Section 4. The dominant uncertainties arise from the theory modelling of the signal and background processes in simulation. Further important uncertainties relate to the luminosity measurement; the selection efficiencies, energy scale and energy resolution of

[2] The p-value is defined as the probability to obtain a value of the test statistic that is at least as high as the observed value, under the hypothesis that is being tested.

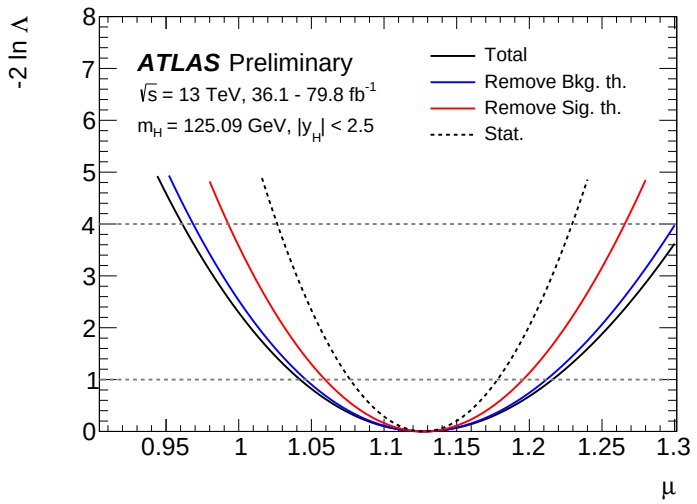

Figure 1: Variations of $-2\log\Lambda(\mu)$ as a function of μ with all systematic uncertainties included (solid black line), with parameters describing theory uncertainties on background processes fixed to their best-fit values (solid blue line), with the same procedure also applied to theory uncertainties on the signal process (solid red line) and all systematic uncertainties (dashed black line). The dotted lines show the levels $-2\log\Lambda(\mu) = 1$ and 4 which are used to define, respectively, the 68% and 95% CL intervals on μ.

electrons and photons; the estimation of lepton yields in heavy-flavour decays, conversions or misidentified hadronic jets; the jet energy scale and resolution, and the identification of heavy-flavour jets. Statistical uncertainties on the numbers of simulated events are also counted among the systematic uncertainties.

Table 3: Summary of the relative uncertainties $\Delta\mu/\mu$ affecting the measurement of the combined global signal strength μ. Only sources of systematic uncertainty associated with relative uncertainties of 0.1% or more are listed. "MC stat." refers to uncertainties due to limited numbers of simulated events.

Uncertainty source	$\frac{\Delta\mu}{\mu}$ [%]
Statistical uncertainties	4.5
Systematic uncertainties (excl. MC stat.)	6.1
Theory uncertainties	4.8
Signal	4.3
Background	2.3
Experimental uncertainties	4.0
Luminosity	2.1
Fake leptons	1.2
Jets, $E_{\mathrm{T}}^{\mathrm{miss}}$	1.3
Flavour tagging	0.9
Background modeling	1.2
Electrons, photons	2.2
Muons	0.3
τ-lepton	0.4
Other	1.5
MC stat. uncertainties	1.5

5.2 Production cross sections

Further information on Higgs boson production is obtained by separately measuring the cross-sections for the ggF, VBF, WH, ZH production mechanisms, and for the combination of $t\bar{t}H$ and tH ($t\bar{t}H$+tH). The latter assumes their relative fractions to be as in the SM. The small contribution from $b\bar{b}H$ is grouped with ggF. The VH process includes ZH production with gluon-gluon initial state ($gg \rightarrow ZH$). Cross-sections are reported in the region $|y_H| < 2.5$ of the Higgs boson rapidity y_H, assuming SM values for its decay branching fractions.

The results are shown in Figure 2 and Table 4. The measured $t\bar{t}H$+tH production cross-section differs from the $t\bar{t}H$ cross-section reported in Ref. [12], after accounting for the difference between the $|y_H| < 2.5$ region used in this note and the inclusive phase space considered in Ref. [12]. This is due in part to the inclusion of tH, which in Ref. [12] is fixed to the SM and not included in the reported $t\bar{t}H$ cross-section, as well as to a better control of systematic effects, in particular photon energy scale and resolution, due to the categories targeting additional processes which are included in this combination.

The leading sources of uncertainty on the production cross-section measurements are summarized in Table 5, with uncertainties computed as described in Section 4. The correlations between the measured cross sections, shown in Figure 3, are significantly reduced with respect to previous analyses [3, 71]. The compatibility between the measurement and the SM prediction corresponds to a p-value of $p_{\mathrm{SM}} = 51\%$.

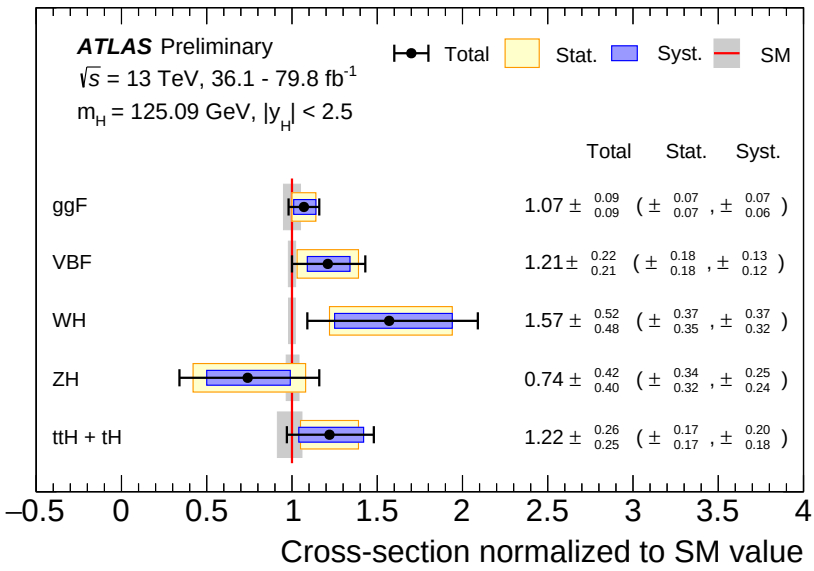

Figure 2: Cross-sections for ggF, VBF, WH, ZH and $t\bar{t}H$+tH normalized to their SM predictions, measured with the assumption of SM branching fractions. The black error bars, blue boxes and yellow boxes show the total, systematic, and statistical uncertainties in the measurements, respectively. The grey bands indicate the theory uncertainties in the cross-section predictions.

Table 4: Best-fit values and uncertainties of the production cross-sections of the Higgs boson, assuming SM values for its decay branching fractions. The total uncertainties are decomposed into components for data statistics (Stat.), experimental systematic uncertainties (Exp.), and theory uncertainties in the modelling of the signal (Sig. th.) and background (Bkg. th.) processes. SM predictions [34] are shown for the cross-section of each production process. The observed (obs.) and expected (exp.) significances of the observed signals relative to the no-signal hypothesis are also shown for all processes except ggF, which was observed in Run 1. For the WH and ZH modes, a combined VH significance is reported assuming the SM value of the ratio of WH to ZH production.

Process	Value	Uncertainty [pb]					SM pred.	Significance
($\|y_H\| < 2.5$)	[pb]	Total	Stat.	Exp.	Sig. th.	Bkg. th.	[pb]	obs. (exp.)
ggF	47.8	± 4.0	$\left(\pm 3.1\right.$	$^{+2.7}_{-2.2}$	± 0.9	$\left.\pm 1.3\right)$	44.7 ± 2.2	-
VBF	4.25	$^{+0.77}_{-0.74}$	$\left(\pm 0.63\right.$	$^{+0.39}_{-0.35}$	$^{+0.25}_{-0.21}$	$\left.^{+0.14}_{-0.11}\right)$	3.515 ± 0.075	6.5 (5.3)
WH	1.89	$^{+0.63}_{-0.58}$	$\left(^{+0.45}_{-0.42}\right.$	$^{+0.29}_{-0.28}$	$^{+0.25}_{-0.16}$	$\left.^{+0.23}_{-0.22}\right)$	1.204 ± 0.024	} 4.1 (3.7)
ZH	0.59	$^{+0.33}_{-0.32}$	$\left(^{+0.27}_{-0.25}\right.$	± 0.14	$^{+0.08}_{-0.02}$	$\left.\pm 0.11\right)$	$0.794^{+0.033}_{-0.027}$	
$t\bar{t}H$+tH	0.71	± 0.15	$\left(\pm 0.10\right.$	± 0.07	$^{+0.05}_{-0.04}$	$\left.^{+0.08}_{-0.07}\right)$	$0.586^{+0.034}_{-0.050}$	5.8 (5.3)

Table 5: Summary of the uncertainties affecting the cross-section measurements. Only systematic uncertainty sources associated with relative uncertainties of 0.1% or more are listed.

Uncertainty source	$\frac{\Delta\sigma_{ggF}}{\sigma_{ggF}}$ [%]	$\frac{\Delta\sigma_{VBF}}{\sigma_{VBF}}$ [%]	$\frac{\Delta\sigma_{WH}}{\sigma_{WH}}$ [%]	$\frac{\Delta\sigma_{ZH}}{\sigma_{ZH}}$ [%]	$\frac{\Delta\sigma_{t\bar{t}H+tH}}{\sigma_{t\bar{t}H+tH}}$ [%]
Total uncertainty	8.8	18	32	55	21
Statistical uncertainties	6.3	15	23	44	14
Systematic unc. (excl. MC stat.)	5.9	9.1	20	27	15
Theory uncertainties	3.3	6.2	16	21	12
Signal	2.1	5.5	11	8.6	5.9
Background	2.6	2.9	11	19	10
Experimental uncertainties	5.0	7.0	9.6	20	9.3
Luminosity	2.2	1.7	1.3	1.9	2.7
Fake leptons	1.6	1.7	0.5	0.8	5.5
Background modelling	2.0	1.4	6.0	8.1	0.9
Flavour tagging	0.8	1.4	4.8	14	1.6
Jets, $E_{\mathrm{T}}^{\mathrm{miss}}$	1.1	5.9	4.9	10	4.6
Electrons, photons	2.5	1.6	2.6	3.5	3.7
Muons	0.4	0.2	0.3	1.0	0.3
τ-lepton	0.2	1.4	0.6	0.7	2.4
Other	2.3	1.2	0.6	1.6	0.4
MC statistical uncertainties	1.5	5.1	9.6	19	4.4

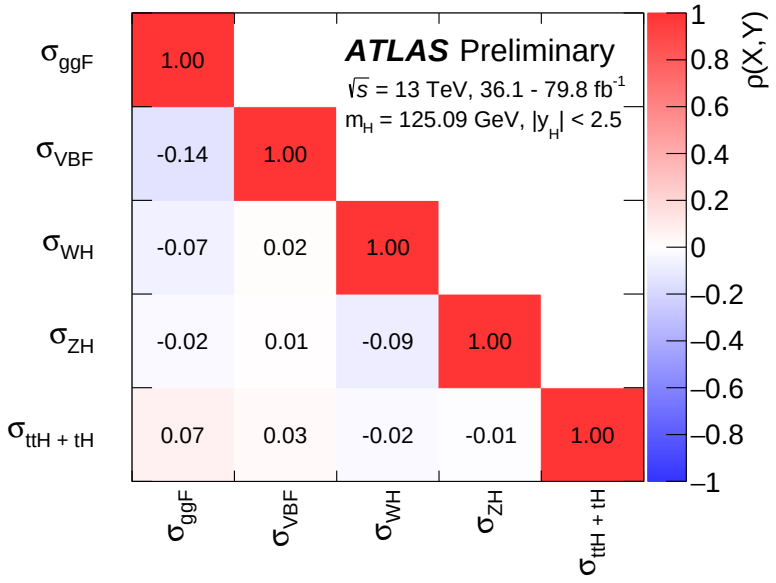

Figure 3: Correlation matrix for the measurement of production cross-sections, as reported in Table 4.

The combined measurement leads to an observed (expected) significance for the vector boson fusion production process of 6.5σ (5.3σ). A significance above 5σ is also observed for $t\bar{t}H$+tH production as well as for ggF. Figure 4 shows the observed likelihood contours in the plane of σ_{ggF} versus σ_{VBF} from individual channels and the combined fit, together with the SM prediction. The cross-sections for the other production modes are profiled. The measured cross-sections are anticorrelated due to contributions from ggF production in the VBF-like selection categories, with a -14% correlation coefficient in the combined measurement.

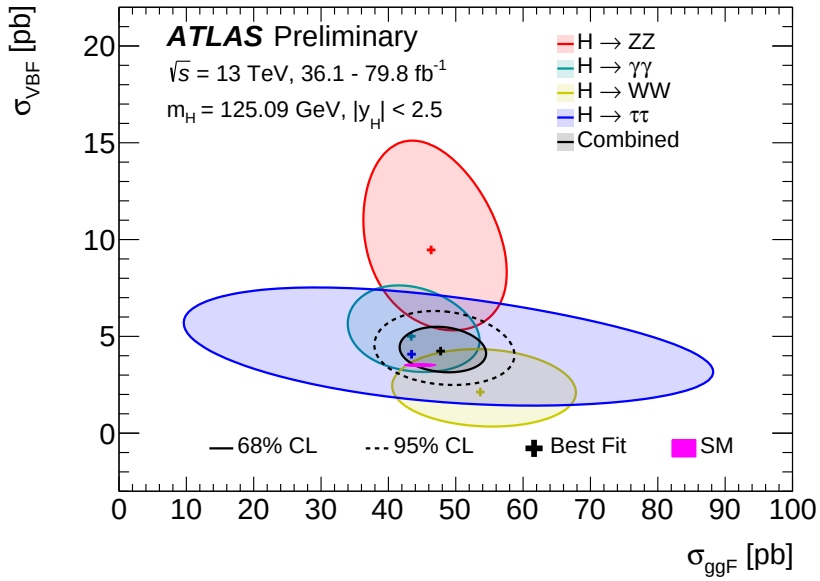

Figure 4: Observed likelihood contours in the plane of σ_{VBF} versus σ_{ggF} from individual channels and the combined fit. Contours for 68% (95%) CL, defined in the asymptotic approximation by $-2\log\Lambda = 2.28$ (5.99), are shown in solid (dashed) lines. The crosses indicate the best-fit value, and the solid ellipse the SM prediction. Higgs boson branching fractions are fixed to their SM values.

Figure 5 shows the combined production cross-section times branching fraction results for ggF, VBF, VH and $t\bar{t}H$+tH production in each relevant decay mode, normalized to their SM predictions. The results are obtained from a simultaneous fit to all decay channels, using as parameters of interest the $(\sigma \times \text{B})_{if}$ for each measured production mode i and decay final state f. Since WH and ZH production cannot be reliably determined in all decay channels, results are presented in terms of their combination only, denoted as VH, assuming the SM value of the ratio of WH to ZH cross-sections. In the $H \to \tau\tau$ decay mode, VH production is not constrained by the data and is thus fixed to its SM prediction. For the same reason, $H \to WW^*$ and $H \to ZZ^*$ decays in $t\bar{t}H$+tH production are considered together as a single measurement, assuming the SM value of the ratio of WW^* to ZZ^* branching ratios.

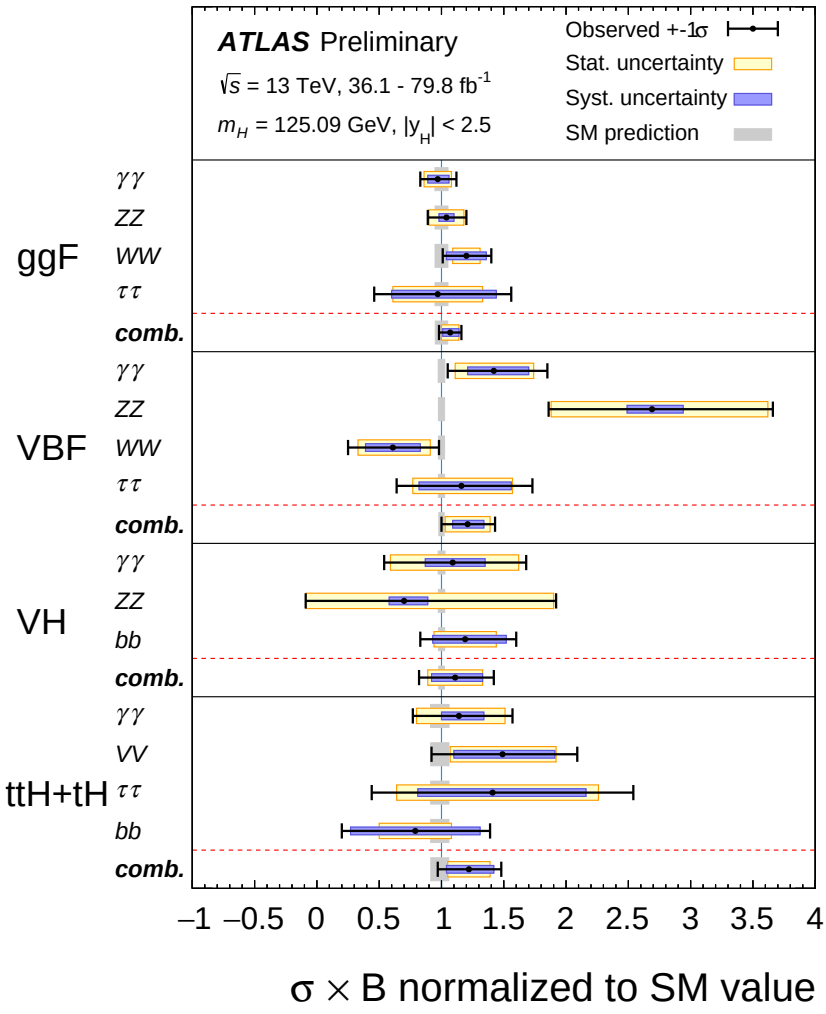

Figure 5: Cross-sections times branching fraction for ggF, VBF, VH and $t\bar{t}H$+tH production in each relevant decay modes, normalized to their SM predictions. The values are obtained from a simultaneous fit to all decay channels. The cross-section for the VH, $H \to \tau\tau$ process is fixed to its SM prediction. Combined results for each production mode are also shown, assuming SM values for the branching ratios into each decay mode. The black error bars, blue boxes and yellow boxes show the total, systematic, and statistical uncertainties in the measurements, respectively. The grey bands show the theory uncertainties in the predictions.

5.3 Ratios of cross-sections and branching fractions

Ratios of cross-sections and of branching fractions are measured using as reference the cross-section of the $gg \to H \to ZZ^*$ process, σ^{ZZ}_{ggF}. The products $(\sigma \times \text{B})_{if}$ of production cross-sections in the process i and branching fraction into the final state f are expressed as

$$(\sigma \times \text{B})_{if} = \sigma^{ZZ}_{\text{ggF}} \cdot \left(\frac{\sigma_i}{\sigma_{\text{ggF}}}\right) \cdot \left(\frac{\text{B}_f}{\text{B}_{ZZ}}\right), \tag{4}$$

in terms of the ratios of the production cross-sections for VBF, WH, ZH and $t\bar{t}H$+tH normalized to that of ggF and the ratios of the branching fractions into the $\gamma\gamma$, WW^*, $b\bar{b}$ and $\tau\tau$ final states normalized to that of $H \to ZZ^*$.

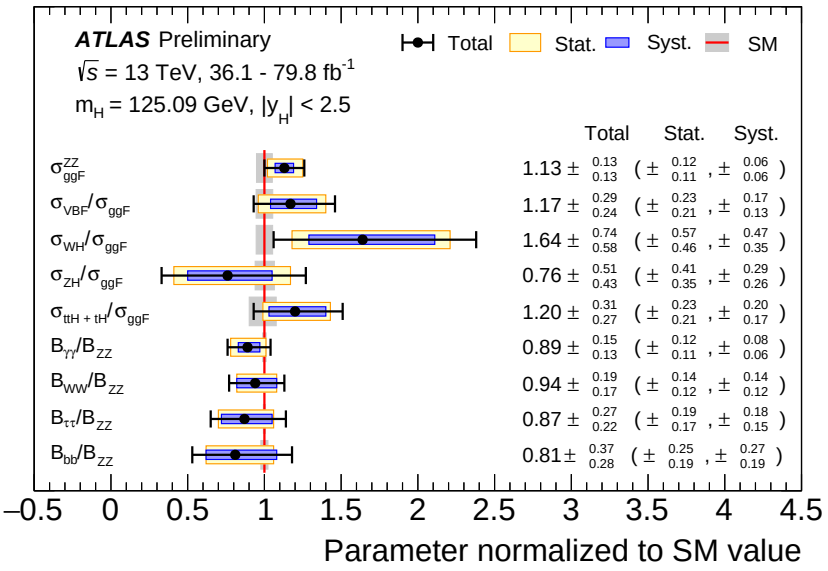

Figure 6: Results of a simultaneous fit for σ^{ZZ}_{ggF}, $\sigma_{VBF}/\sigma_{\text{ggF}}$, $\sigma_{WH}/\sigma_{\text{ggF}}$, $\sigma_{ZH}/\sigma_{\text{ggF}}$, $\sigma_{t\bar{t}H+tH}/\sigma_{\text{ggF}}$, $B_{\gamma\gamma}/B_{ZZ}$, B_{WW}/B_{ZZ}, $B_{\tau\tau}/B_{ZZ}$, and B_{bb}/B_{ZZ}. The fit results are normalized to the SM predictions. The black error bars, blue boxes and yellow boxes show the total, systematic, and statistical uncertainties in the measurements, respectively. The grey bands show the theory uncertainties in the predictions.

Figure 6 and Table 6 show the measurements of σ^{ZZ}_{ggF}, $\sigma_{VBF}/\sigma_{\text{ggF}}$, $\sigma_{WH}/\sigma_{\text{ggF}}$, $\sigma_{ZH}/\sigma_{\text{ggF}}$, $\sigma_{t\bar{t}H+tH}/\sigma_{\text{ggF}}$, $B_{\gamma\gamma}/B_{ZZ}$, B_{WW}/B_{ZZ}, $B_{\tau\tau}/B_{ZZ}$, and B_{bb}/B_{ZZ}. The correlations between the measured parameters are summarized in Figure 7. The compatibility between the measurements and the SM predictions corresponds to a p-value of $p_{\text{SM}} = 83\%$.

Table 6: Best-fit values and uncertainties of $\sigma^{ZZ}_{\mathrm{ggF}}$, together with ratios of production cross-sections normalized to σ_{ggF}, and ratios of branching fractions normalized to B_{ZZ}. Uncertainties in the SM predictions are computed following the same method as for Ref. [3].

Quantity	Value	Uncertainty					SM prediction
		Total	Stat.	Exp.	SigTheo.	BkgTheo.	
$\sigma^{ZZ}_{\mathrm{ggF}}$ [pb]	1.33	±0.15	$^{+0.14}_{-0.13}$	±0.06	$^{+0.02}_{-0.01}$	$^{+0.04}_{-0.02}$	1.181 ± 0.061
$\sigma_{VBF}/\sigma_{\mathrm{ggF}}$	0.092	$^{+0.023}_{-0.019}$	$^{+0.018}_{-0.017}$	$^{+0.010}_{-0.009}$	$^{+0.006}_{-0.005}$	$^{+0.006}_{-0.004}$	0.0786 ± 0.0043
$\sigma_{WH}/\sigma_{\mathrm{ggF}}$	0.044	$^{+0.020}_{-0.016}$	$^{+0.015}_{-0.012}$	$^{+0.009}_{-0.007}$	$^{+0.004}_{-0.003}$	$^{+0.008}_{-0.006}$	$0.0269^{+0.0014}_{-0.0015}$
$\sigma_{ZH}/\sigma_{\mathrm{ggF}}$	0.0135	$^{+0.0091}_{-0.0076}$	$^{+0.0073}_{-0.0062}$	$^{+0.0039}_{-0.0035}$	$^{+0.0014}_{-0.0005}$	$^{+0.0032}_{-0.0028}$	$0.0177^{+0.0012}_{-0.0011}$
$\sigma_{t\bar{t}H+tH}/\sigma_{\mathrm{ggF}}$	0.0157	$^{+0.0041}_{-0.0035}$	$^{+0.0030}_{-0.0028}$	$^{+0.0020}_{-0.0017}$	$^{+0.0010}_{-0.0008}$	$^{+0.0013}_{-0.0012}$	$0.0131^{+0.0010}_{-0.0013}$
$\mathrm{B}_{\gamma\gamma}/\mathrm{B}_{ZZ}$	0.076	$^{+0.013}_{-0.011}$	$^{+0.010}_{-0.009}$	$^{+0.006}_{-0.005}$	$^{+0.003}_{-0.002}$	±0.002	0.08595 ± 0.00095
$\mathrm{B}_{WW}/\mathrm{B}_{ZZ}$	7.7	$^{+1.5}_{-1.4}$	$^{+1.1}_{-1.0}$	$^{+0.8}_{-0.7}$	$^{+0.4}_{-0.3}$	$^{+0.7}_{-0.6}$	$8.15\pm < 0.01$
$\mathrm{B}_{\tau\tau}/\mathrm{B}_{ZZ}$	2.06	$^{+0.64}_{-0.52}$	$^{+0.45}_{-0.40}$	$^{+0.36}_{-0.31}$	$^{+0.21}_{-0.12}$	$^{+0.14}_{-0.09}$	2.369 ± 0.017
$\mathrm{B}_{bb}/\mathrm{B}_{ZZ}$	17.8	$^{+8.1}_{-6.2}$	$^{+5.5}_{-4.2}$	$^{+3.5}_{-2.4}$	$^{+1.5}_{-1.1}$	$^{+4.4}_{-3.3}$	22.00 ± 0.51

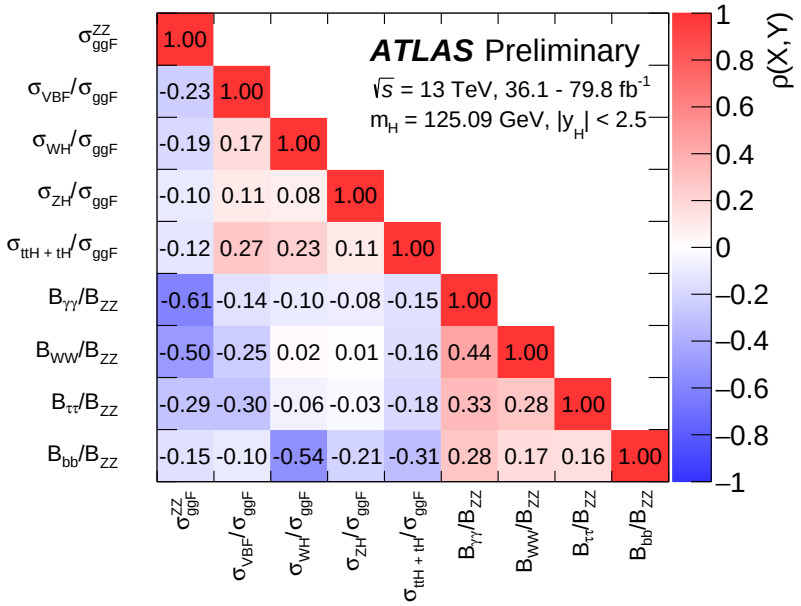

Figure 7: Correlation matrix for the measured values of the parameters shown in Table 6.

5.4 Results in the κ framework

The κ framework expresses Higgs boson interactions using multiplicative modifiers to SM cross-sections and partial widths, leading to the parameterization [22]

$$(\sigma \times \mathrm{B})_{if} = \kappa_i^2 \sigma_i^{\mathrm{SM}} \frac{\kappa_f^2 \Gamma_f^{\mathrm{SM}}}{\kappa_H^2 \Gamma_H^{\mathrm{SM}}}, \tag{5}$$

where σ_i^{SM} is the SM production cross-section, and Γ_H^{SM} and Γ_f^{SM} are the SM values of the total Higgs boson width and the partial width into the final state f, respectively. The modifiers κ_i^2 and κ_f^2, applied, respectively, to the production cross-sections and partial widths, can be expressed in terms of κ_X modifiers applied to the tree-level couplings between the Higgs boson and other SM particles. The couplings Hgg and $H\gamma\gamma$ to gluons and photons, which arise from loop processes in the SM, are modified in the same way using modifiers denoted as κ_g and κ_γ, respectively. An additional parameter $\mathrm{B_{BSM}}$ is also introduced to describe BSM effects in the branching ratios of Higgs boson decays to invisible and undetected states. These states are defined as in Ref. [3] as decays into final states that are either undetectable by ATLAS or not covered by the analyses presented in this note, or modifications to the branching fractions of channels such as $H \to c\bar{c}$ [72, 73] which have not yet been directly measured. In the absence of BSM contributions in the Hgg and $H\gamma\gamma$ interactions, the effective modifiers κ_g and κ_γ can be expressed in terms of the κ_X. Similarly, the modifier of the Higgs boson total width κ_H can be calculated from the other κ parameters and $\mathrm{B_{BSM}}$. These relations are summarized in Table 7. Interference effects are present in particular in the ggF, $gg \to ZH$ and tH production and the $H \to \gamma\gamma$ decay processes.

The individual channel measurements are combined to obtain confidence intervals for the κ modifiers using various assumptions on the relationships between the Higgs boson couplings. Theory uncertainties on SM predictions are included as for the signal-strength measurement described in Section 5.1.

Table 7: Multiplicative modifiers applied to Higgs boson production cross-section and decay partial widths, parameterized as a function of the couplings modifiers κ and the parameter B_{BSM} discussed in the text. The modifications to ggF, $H \to \gamma\gamma$ and the total width can be expressed by using either effective modifiers, listed in the second column, or expressions derived from other modifiers under SM assumptions, listed in the third column.

Production	Effective modifier	Resolved modifier
σ_{ggF}	κ_g^2	$1.04\,\kappa_t^2 + 0.002\,\kappa_b^2 - 0.04\,\kappa_t\kappa_b$
σ_{VBF}	-	$0.73\,\kappa_W^2 + 0.27\,\kappa_Z^2$
$\sigma_{qq/qg\to ZH}$	-	κ_Z^2
$\sigma_{gg\to ZH}$	-	$2.46\,\kappa_Z^2 + 0.46\,\kappa_t^2 - 1.90\,\kappa_Z\kappa_t$
σ_{WH}	-	κ_W^2
$\sigma_{t\bar{t}H}$	-	κ_t^2
σ_{tHW}	-	$2.91\,\kappa_t^2 + 2.31\,\kappa_W^2 - 4.22\,\kappa_t\kappa_W$
σ_{tHq}	-	$2.63\,\kappa_t^2 + 3.58\,\kappa_W^2 - 5.21\,\kappa_t\kappa_W$
$\sigma_{b\bar{b}H}$	-	κ_b^2
Partial decay width	**Effective modifier**	**Resolved modifier**
$\Gamma_{\gamma\gamma}$	κ_γ^2	$1.59\,\kappa_W^2 + 0.07\,\kappa_t^2 - 0.67\,\kappa_W\kappa_t$
Γ_{ZZ}	-	κ_Z^2
Γ_{WW}	-	κ_W^2
$\Gamma_{\tau\tau}$	-	κ_τ^2
Γ_{bb}	-	κ_b^2
$\Gamma_{\mu\mu}$	-	κ_μ^2
Γ_{gg}	κ_g^2	$1.11\,\kappa_t^2 + 0.01\,\kappa_b^2 - 0.12\,\kappa_t\kappa_b$
$\Gamma_{Z\gamma}$	$\kappa_{(Z\gamma)}^2$	$1.12\,\kappa_W^2 - 0.12\,\kappa_W\kappa_t$
Total width	**Efective modifier**	**Resolved modifier**
Γ_H	κ_H^2	$(0.58\,\kappa_b^2 + 0.22\,\kappa_W^2 + 0.08\,\kappa_g^2 + 0.06\,\kappa_\tau^2 + 0.03\,\kappa_Z^2 + 0.03\,\kappa_c^2$ $+0.0023\,\kappa_\gamma^2 + 0.0015\,\kappa_{(Z\gamma)}^2 + 0.0004\,\kappa_s^2 + 0.00022\,\kappa_\mu^2)/(1 - B_{BSM})$

5.4.1 Modifications to fermion and gauge boson couplings

In this model all couplings to fermions are assumed to scale with a single modifier κ_F, and couplings to W and Z bosons with a modifier κ_V. The effective couplings κ_g and κ_γ and the total width modifier κ_H are expressed in terms of κ_F and κ_V as given in Table 7, assuming $B_{BSM} = 0$. The cross-sections for the ggF and $t\bar{t}H$ production processes scale with κ_F^2, while those of VBF and VH productions are proportional to κ_V^2. The $H \to ZZ^*$ and $H \to WW^*$ branching fractions are proportional to κ_V^2, while those of $H \to b\bar{b}$ and $H \to \tau\tau$ scale with κ_F^2. The $H \to \gamma\gamma$ branching fraction depends on a combination of κ_V^2, κ_F^2, and $\kappa_V\kappa_F$ due to contributions from top-quark loops, W-boson loops and their interference to the decay process. The κ_V parameter is assumed to be positive without loss of generality, and κ_F is assumed to be positive since its negative range was excluded by previous measurements [3]. The fit results are summarized in Figure 8 with contours in the (κ_F, κ_V) plane, from individual channels and the combined fit. The best-fit values and uncertainties are

$$\kappa_V = 1.06^{+0.04}_{-0.04}$$
$$\kappa_F = 1.05^{+0.09}_{-0.09}.$$

A 45% correlation is observed between the two quantities. The compatibility of the measurement with the SM prediction corresponds to a p-value of $p_{SM} = 31\%$.

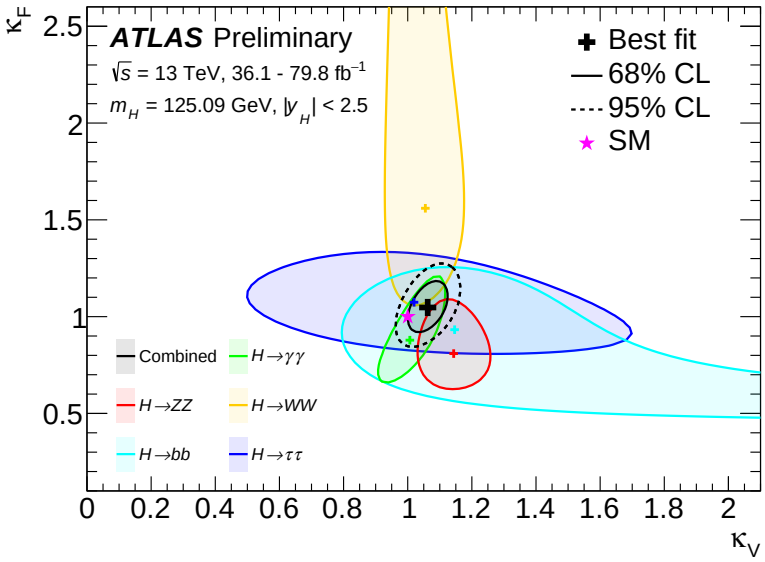

Figure 8: Observed contours at 68% and 95% CL in the (κ_F, κ_V) plane, defined in the asymptotic approximation by $-2\log\Lambda = 2.28$ and 5.99, respectively, for individual channels and the combined fit. The crosses indicate the best-fit values and the star the SM prediction.

5.4.2 Modifications to effective photon and gluon couplings with and without BSM contributions in decays

In these models the modifiers κ_g and κ_γ are considered as free parameters, without the assumption that only SM sources contribute to the loops. Other κ parameters are fixed to 1, corresponding to SM values

of the corresponding couplings. Two models are considered. In the first model, B_{BSM} is assumed to be zero. The best-fit values and uncertainties are then

$$\kappa_g = 1.05^{+0.06}_{-0.06}$$
$$\kappa_\gamma = 1.00^{+0.07}_{-0.06}.$$

Two-dimensional likelihood contours in the $(\kappa_\gamma, \kappa_g)$ plane are shown in Figure 9. The correlation between the two quantities is estimated to be -44%, due in part to the fact that their product is constrained by the rate of $H \to \gamma\gamma$ in the gluon-gluon fusion channel. The compatibility of the measurement with the SM prediction corresponds to a p-value of $p_{SM} = 71\%$.

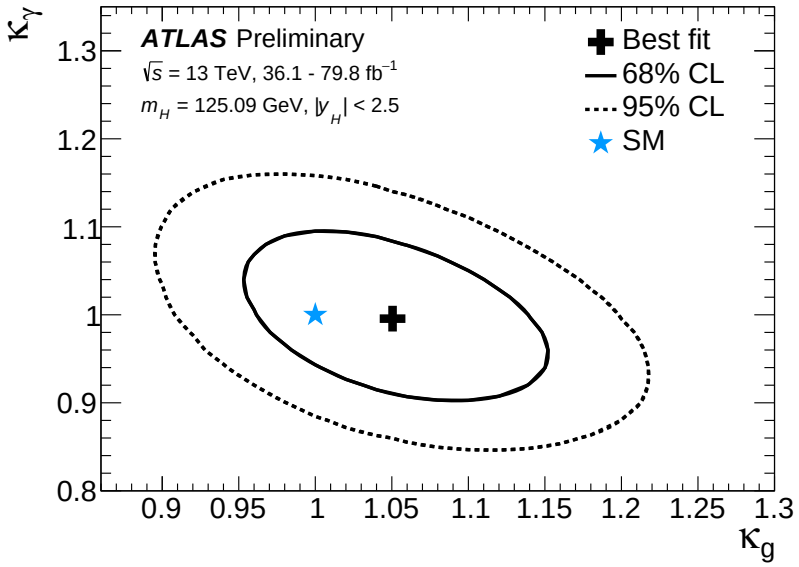

Figure 9: Observed contours at 68% and 95% CL in the $(\kappa_\gamma, \kappa_g)$ plane, defined in the asymptotic approximation by $-2\log\Lambda = 2.28$ and 5.99, respectively. The cross indicates the best-fit value and the star the SM prediction.

In the second model, the B_{BSM} parameter is left free in the fit. The results are

$$\kappa_g = 1.05^{+0.07}_{-0.06}$$
$$\kappa_\gamma = 1.00^{+0.07}_{-0.06}$$
$$B_{BSM} < 0.13 \text{ at } 95\% \text{ CL}.$$

5.4.3 Parameterization assuming SM structure of the loops and no BSM contributions in decays

In this model separate modifiers κ_W and κ_Z are considered for couplings to W and Z bosons, respectively. Separate couplings κ_t, κ_b, κ_τ and κ_μ are also introduced, respectively, for couplings to top and charm quarks, bottom and strange quarks, τ leptons, and muons. The results of the $H \to \mu\mu$ analysis are included for this specific case. SM values are assumed for couplings to first-generation fermions, and B_{BSM} is assumed to be zero. All couplings are assumed to be positive. The results are shown in Table 8.

Reduced coupling strength modifiers are defined for fermions ($F = t, b, \tau, \mu$) as $\kappa_F \frac{m_F}{v}$, and for gauge bosons ($V = W, Z$) as $\sqrt{\kappa_V}\frac{m_V}{v}$, where κ_F (κ_V) is the coupling modifier, m_F (m_V) is the mass of the

Table 8: Fit results for κ_Z, κ_W, κ_b, κ_t, κ_τ and κ_μ. All parameters are defined to be unity in the SM, and are assumed to be positive.

Parameter	Result
κ_Z	$1.07^{+0.11}_{-0.10}$
κ_W	1.04 ± 0.10
κ_b	$1.00^{+0.24}_{-0.22}$
κ_t	$1.03^{+0.12}_{-0.11}$
κ_τ	$1.04^{+0.17}_{-0.16}$
κ_μ	< 1.63 at 95% CL.

fermion (boson), and $v = 246\,\text{GeV}$ is the vacuum expectation value of the Higgs field. The SM prediction is given by m/v for both cases, where m is the mass of the fermion or boson. Reduced couplings strengths are shown as a function of mass in Figure 10.

The compatibility of the measurement with the SM prediction corresponds to a p-value of $p_{\text{SM}} = 79\%$.

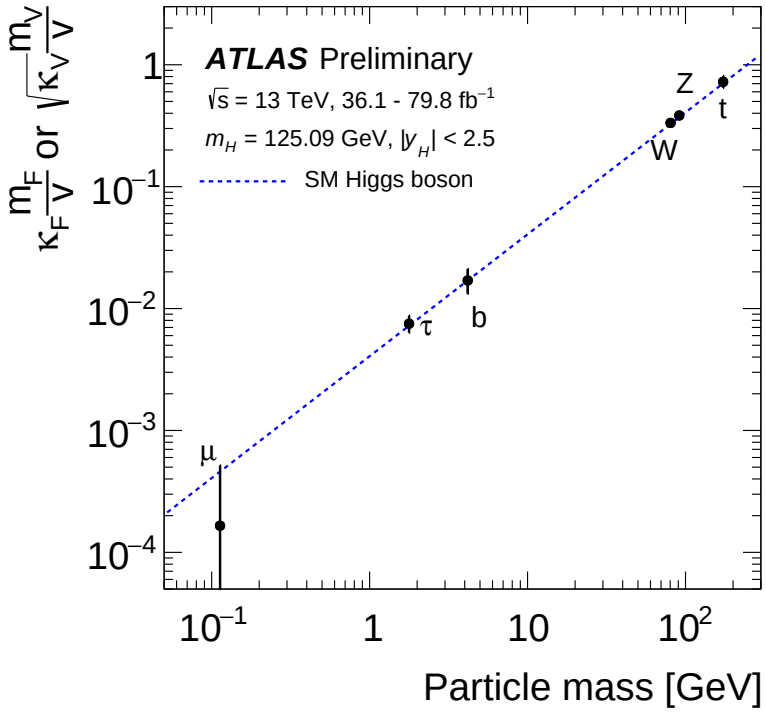

Figure 10: Reduced coupling strength modifiers $\kappa_F \frac{m_F}{v}$ for fermions ($F = t, b, \tau, \mu$) and $\sqrt{\kappa_V}\frac{m_V}{v}$ for weak gauge bosons ($V = W, Z$) as a function of their masses m_F and m_V, respectively, and the vacuum expectation value of the Higgs field $v = 246\,\text{GeV}$. The SM prediction for both cases is also shown (dotted line). The couplings modifiers κ_F and κ_V are measured assuming no BSM contributions to the Higgs boson decays, and the SM structure of loop processes such as ggF, $H \to \gamma\gamma$ and $H \to gg$.

5.4.4 Parameterization including effective photon and gluon couplings with and without BSM contributions in decays

The two models considered in this section are based on the same parameterization as the one in Section 5.4.3 but the ggF, $H \to gg$ and $H \to \gamma\gamma$ loop processes are parameterized using the κ_g and κ_γ modifiers in the same way as for the model of Section 5.4.2.

In the first model, no BSM contributions to the total width are considered ($B_{BSM} = 0$). The measured parameters are κ_Z, κ_W, κ_b, κ_t, κ_τ, κ_γ and κ_g. The sign of κ_t can be either positive or negative, while κ_Z is assumed to be positive without loss of generality. The other parameters are also assumed to be positive.

In the second model, BSM contributions to the total width are included through the parameter B_{BSM}, and constrained by assuming $B_{BSM} \geq 0$ and $\kappa_{W,Z} \leq 1$. The latter condition holds true for a broad class of extensions of the SM and disfavors large values of B_{BSM} [22].

The results of both models are summarized in Table 9 and Figure 11. In the model with B_{BSM} included as a free parameter, an upper limit of $B_{BSM} = 0.26$ at 95% CL is obtained, compared to an expected upper

limit of 0.37. In the model with $B_{BSM} = 0$, the compatibility of the measurement with the SM prediction corresponds to a p-value of $p_{SM} = 87\%$.

Table 9: Fit results for Higgs boson coupling modifiers per particle type with effective photon and gluon couplings and either (a) $B_{BSM} = 0$ or (b) B_{BSM} included as a free parameter. The SM corresponds to $B_{BSM} = 0$ and all κ parameters set to unity. All parameters except κ_t are assumed to be positive. For (b), the conditions $\kappa_{W,Z} \leq 1$ are also applied.

Parameter	(a) no BSM	(b) with BSM
κ_Z	1.07 ± 0.10	restricted to $\kappa_Z \leq 1$
κ_W	1.07 ± 0.11	restricted to $\kappa_W \leq 1$
κ_b	$0.97^{+0.24}_{-0.22}$	$0.85^{+0.13}_{-0.14}$
κ_t	$1.09^{+0.15}_{-0.14}$	$1.05^{+0.14}_{-0.13}$
κ_τ	$1.02^{+0.17}_{-0.16}$	0.95 ± 0.13
κ_γ	$1.02^{+0.09}_{-0.12}$	$0.98^{+0.05}_{-0.08}$
κ_g	$1.00^{+0.12}_{-0.11}$	$0.97^{+0.10}_{-0.09}$
B_{BSM}	-	< 0.26 at 95% CL

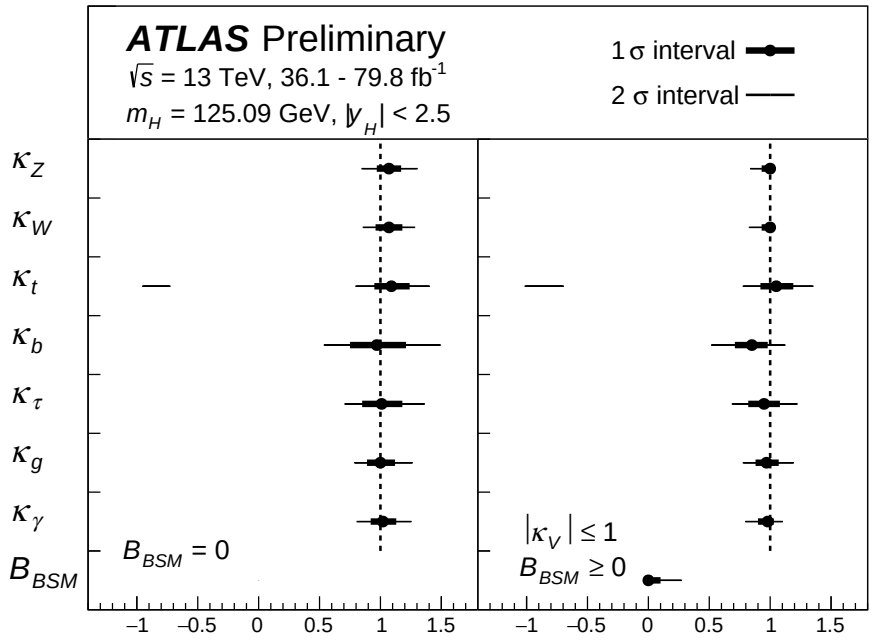

Figure 11: Best-fit values and uncertainties of Higgs boson coupling modifiers per particle type with effective photon and gluon couplings and either $B_{BSM} = 0$ (left), or B_{BSM} included as a free parameter (right). The SM corresponds to $B_{BSM} = 0$ and all κ parameters set to unity. All parameters except κ_t are assumed to be positive. In the model with B_{BSM} included as a free parameter, the conditions $\kappa_{W,Z} \leq 1$ are also applied and an upper limit on B_{BSM} is reported.

5.4.5 Parameterization using ratios of coupling modifiers

Finally, a model based on ratios of coupling modifiers is defined analogously to the cross-section ratio model of Section 5.3. The model parameters are the scaling factors defined in Table 10. The parameterization requires no assumption on the total width of the Higgs boson. All parameters are assumed to be positive. The results are summarized in Table 10 and Figure 12. The compatibility between the measurement and the SM prediction corresponds to a p-value of $p_{SM} = 86\%$.

Table 10: Best-fit values and uncertainties of ratios of coupling modifiers. The second column provides the expression of the measured parameters in terms of the coupling modifiers defined in previous sections. All parameters are defined to be unity in the SM.

Parameter	Definition in terms of κ modifiers	Result
κ_{gZ}	$\kappa_g\kappa_Z/\kappa_H$	1.06 ± 0.07
λ_{tg}	κ_t/κ_g	$1.09^{+0.14}_{-0.14}$
λ_{Zg}	κ_Z/κ_g	$1.06^{+0.14}_{-0.13}$
λ_{WZ}	κ_W/κ_Z	$0.99^{+0.09}_{-0.08}$
$\lambda_{\gamma Z}$	κ_γ/κ_Z	$0.95^{+0.08}_{-0.07}$
$\lambda_{\tau Z}$	κ_τ/κ_Z	0.95 ± 0.13
λ_{bZ}	κ_b/κ_Z	$0.91^{+0.17}_{-0.16}$

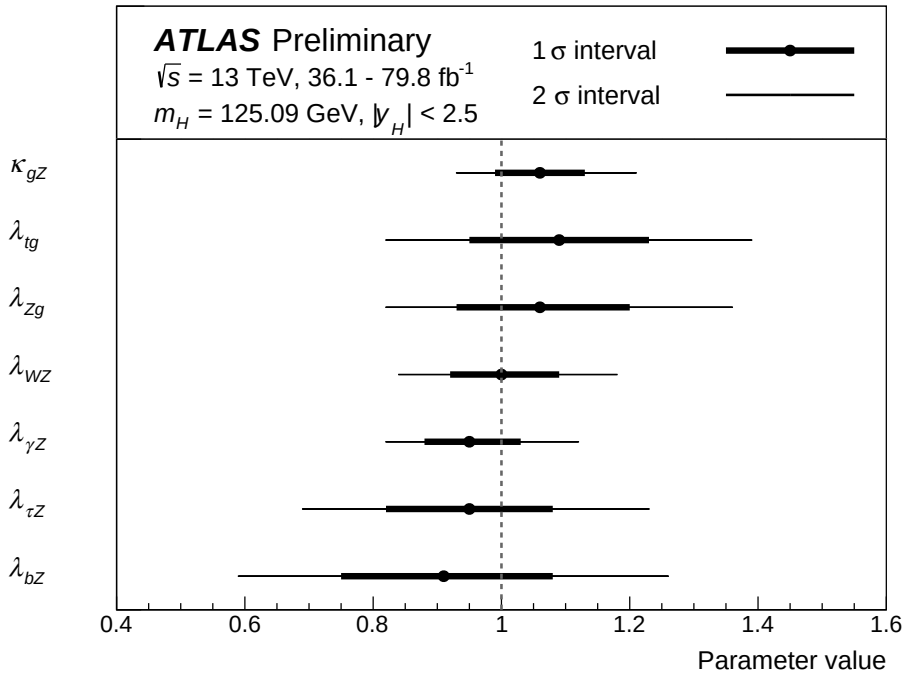

Figure 12: Measured ratios of coupling modifiers. The dashed line indicates the SM value of unity for each parameter.

5.5 Constraints on New Phenomena

Two Higgs doublet Models (2HDMs) [22, 74–76] and Supersymmetry [77–82] are promising scenarios of physics beyond the SM. The measurements are interpreted in these benchmark models, providing indirect limits on their parameters that are complementary to those obtained by direct searches for new particles. The interpretations presented in this section follow the procedure discussed in Ref. [23].

5.5.1 Two Higgs doublet model

In 2HDMs, the SM Higgs sector is extended by introducing an additional complex isodoublet scalar field with weak hypercharge one. Four types of 2HDMs satisfy the Paschos-Glashow-Weinberg condition [83, 84], which prevents the appearance of tree-level flavor-changing neutral currents:

- Type I: one Higgs doublet couples to vector bosons, while the other one couples to fermions. The first doublet is 'fermiophobic' in the limit where the two Higgs doublets do not mix.
- Type II: one Higgs doublet couples to up-type quarks and the other one to down-type quarks and charged leptons.
- Lepton-specific: the Higgs bosons have the same couplings to quarks as in the Type I model and to charged leptons as in Type II.
- Flipped: the Higgs bosons have the same couplings to quarks as in the Type II model and to charged leptons as in Type I.

The observed Higgs boson is identified with the light CP-even neutral scalar h predicted by 2HDMs, and its accessible production and decay modes are assumed to be the same as those of the SM Higgs boson. Its couplings to vector bosons, up-type quarks, down-type quarks and leptons relative to the corresponding SM predictions are expressed as functions of the mixing angle of h with the heavy CP-even neutral scalar, α, and the ratio of the vacuum expectation values of the Higgs doublets, $\tan\beta$.

Figure 13 shows the regions of the $(\cos(\beta-\alpha), \tan\beta)$ plane that are excluded at a confidence level of 95 % or higher, for each of the four types of 2HDMs. The expected exclusion limits in the SM hypothesis are also overlaid. The data are consistent with the alignment limit [76] at $\cos(\beta-\alpha) = 0$, in which the couplings of h match those of the SM Higgs boson, within one standard deviation or better in each of the tested models. The allowed regions also include narrow, curved 'petal' regions at positive $\cos(\beta-\alpha)$ and moderate $\tan\beta$ in the Type II, Lepton-specific, and Flipped models. These correspond to regions with $\cos(\beta+\alpha) \approx 0$, for which some fermion couplings have the same magnitude as in the SM, but the opposite sign.

5.5.2 Simplified Minimal Supersymmetric Standard Model

The Minimal Supersymmetric Standard Model (MSSM) [85–87] is a realization of a Type II 2HDM. As a benchmark, a simplified MSSM model in which the Higgs boson is identified with the light CP-even scalar h, termed hMSSM [88–90], is studied. The assumptions made by this model are discussed in Ref. [23]. The production and decay modes accessible to h are assumed to be the same as those of the SM Higgs boson.

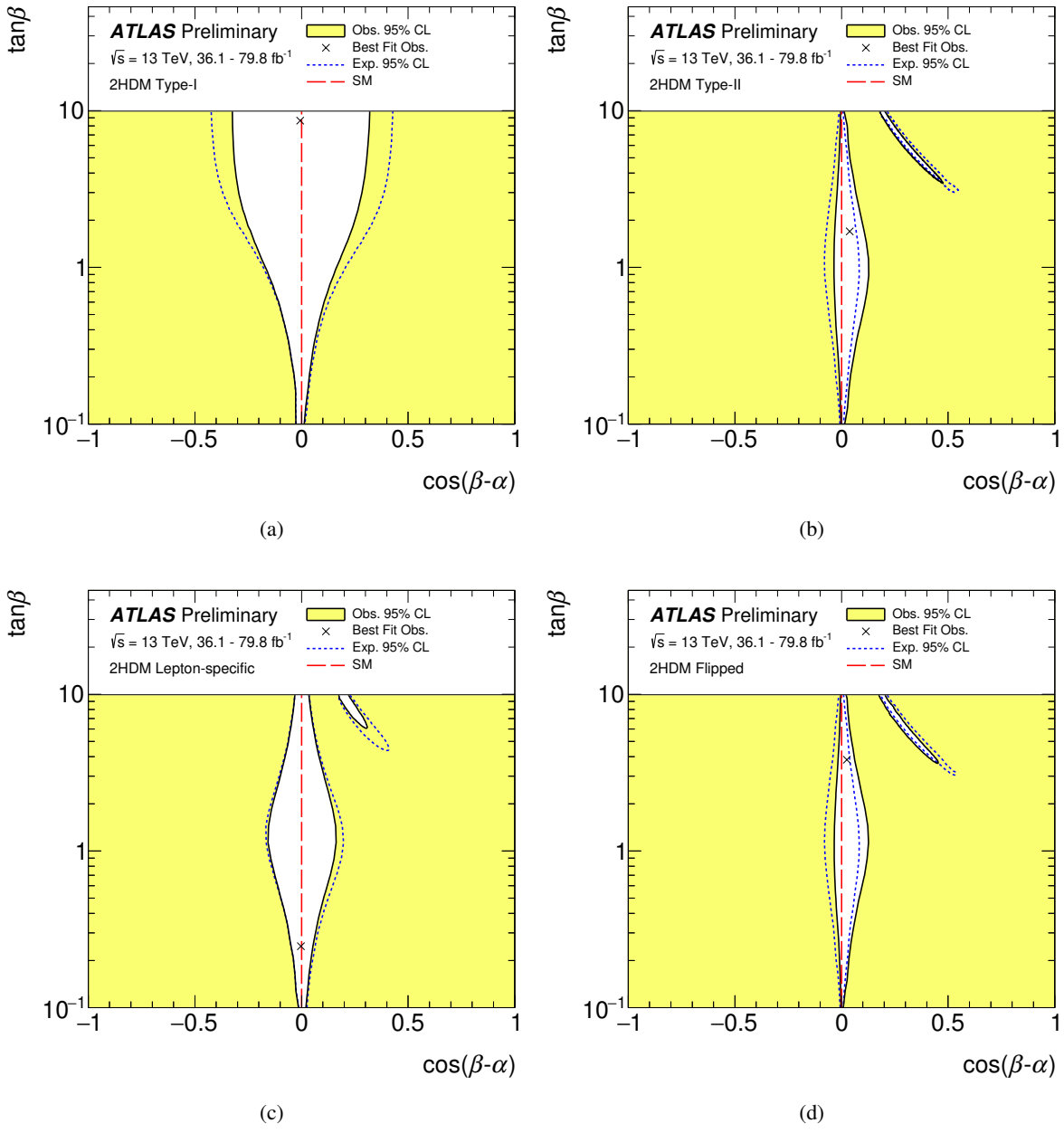

Figure 13: Regions of the $(\cos(\beta-\alpha), \tan\beta)$ plane of four types of 2HDMs excluded by fits to the measured rates of Higgs boson production and decays. Contours at 95% CL, defined in the asymptotic approximation by $-2\log\Lambda = 5.99$, are drawn for both the data and the expectation for the SM Higgs sector. The cross in each plot marks the observed best-fit value. The regions of compatibility extend to larger and smaller $\tan\beta$ values, but with a correspondingly narrower range of $\cos(\beta-\alpha)$. The angles α and β are taken to satisfy $0 \leq \beta \leq \pi/2$ and $0 \leq \beta-\alpha \leq \pi$ without loss of generality. The alignment limit at $\cos(\beta-\alpha) = 0$, in which all Higgs boson couplings take their SM values, is indicated by the dashed red line.

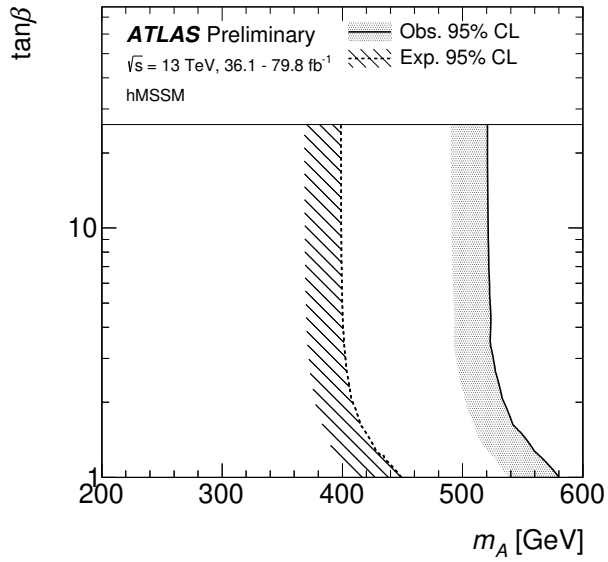

Figure 14: Regions of the $[m_A, \tan\beta]$ plane in the hMSSM excluded by fits to the measured rates of Higgs boson production and decays. Likelihood contours at 95% CL, defined in the asymptotic approximation by $-2\log\Lambda = 5.99$, are drawn for both the data and the expectation of the SM Higgs sector. The regions to the left of the solid contour are excluded. The decoupling limit, in which all Higgs boson couplings tend to their SM value, corresponds to $m_A \to \infty$. The hMSSM is a good approximation of the MSSM only for moderate values of $\tan\beta$. For $\tan\beta \gtrsim 10$ the scenario is approximate due to missing supersymmetry corrections in the Higgs boson coupling to b-quarks, and for $\tan\beta$ of $O(1)$ the precision of the approximation depends on m_A [34].

The Higgs boson couplings to vector bosons, up-type fermions and down-type fermions relative to the corresponding SM predictions are expressed as functions of the ratio of the vacuum expectation values of the Higgs doublets, $\tan\beta$, and the masses of the CP-odd scalar (m_A), the Z boson, and of h.

Figure 14 shows the regions of the hMSSM parameter space that are indirectly excluded by the measurement of the Higgs boson production and decay rates. The data are consistent with the SM decoupling limit at large m_A, where h couplings tend to those of the SM Higgs boson. The observed (expected) lower limit at 95 % CL on the CP-odd Higgs boson mass is at least $m_A > 520\,\text{GeV}$ ($m_A > 400\,\text{GeV}$) for $1 \leq \tan\beta \leq 25$, increasing to $m_A > 580\,\text{GeV}$ ($m_A > 450\,\text{GeV}$) at $\tan\beta = 1$.

6 Conclusions

Measurements of Higgs boson production cross-sections and branching ratios have been performed using up to $79.8\,\text{fb}^{-1}$ of proton-proton collision data produced by the LHC at $\sqrt{s} = 13\,\text{TeV}$ and recorded by the ATLAS detector. They are obtained in the combination of measurements obtained in the $H \to \gamma\gamma$, $H \to ZZ^*$, $H \to WW^*$, $H \to \tau\tau$, $H \to b\bar{b}$ and $H \to \mu\mu$ decay channels.

The global signal strength is determined to be $\mu = 1.13^{+0.09}_{-0.08}$.

The Higgs boson production cross-sections within the region $|y_H| < 2.5$ are measured in a combined fit for the gluon-gluon fusion process, vector-boson fusion, the associated production with a W or Z boson and the associated production with top quarks, assuming the SM Higgs boson branching fractions.

The combined measurement leads to an observed (expected) significance for the vector-boson fusion production process of 6.5σ (5.3σ), an observation of this process by the ATLAS experiment following its observation in the combination of ATLAS and CMS measurements using the Run 1 dataset.

Removing the SM assumption on branching fractions, a combined fit is performed for the cross-section of the $gg \to H \to ZZ^*$ process, ratios of production cross-sections relative to that of ggF production, and ratios of branching fraction relative to that of $H \to ZZ^*$.

The observed Higgs boson yields are used to obtain confidence intervals for κ modifiers to the couplings of the SM Higgs boson to fermions, weak vector bosons, gluons, and photons, and to the branching ratio of the Higgs boson to invisible and undetected decay modes. No significant deviation from the Standard Model predictions is observed.

Finally, the results are interpreted in the context of two-Higgs doublet models and the hMSSM. Constraints are set in the $(m_A, \tan\beta)$ plane of the hMSSM and the $(\cos(\beta-\alpha), \tan\beta)$ plane in 2HDM Type-I, Type-II, Lepton-specific and Flipped models.

References

[1] ATLAS Collaboration, *Observation of a new particle in the search for the Standard Model Higgs boson with the ATLAS detector at the LHC*, Phys. Lett. B **716** (2012) 1, arXiv: 1207.7214 [hep-ex].

[2] CMS Collaboration, *Observation of a new boson at a mass of 125 GeV with the CMS experiment at the LHC*, Phys. Lett. B **716** (2012) 30, arXiv: 1207.7235 [hep-ex].

[3] ATLAS and CMS Collaborations, *Measurements of the Higgs boson production and decay rates and constraints on its couplings from a combined ATLAS and CMS analysis of the LHC pp collision data at $\sqrt{s}$ = 7 and 8 TeV*, JHEP **08** (2016) 045, arXiv: 1606.02266 [hep-ex].

[4] ATLAS Collaboration, *Measurements of Higgs boson properties in the diphoton decay channel using 80 fb^{-1} of pp collision data at $\sqrt{s}$ = 13 TeV with the ATLAS detector*, ATLAS-CONF-2018-028, URL: http://cdsweb.cern.ch/record/2628771.

[5] ATLAS Collaboration, *Measurements of the Higgs boson production, fiducial and differential cross sections in the 4ℓ decay channel at $\sqrt{s}$ = 13 TeV with the ATLAS detector*, ATLAS-CONF-2018-018, URL: http://cds.cern.ch/record/2621479.

[6] ATLAS Collaboration, *Measurement of gluon fusion and vector boson fusion Higgs boson production cross-sections in the $H \to WW^* \to e\nu\mu\nu$ decay channel in pp collisions at $\sqrt{s}$ = 13 TeV with the ATLAS detector*, ATLAS-CONF-2018-004, URL: http://cds.cern.ch/record/2308392.

[7] ATLAS Collaboration, *Cross-section measurements of the Higgs boson decaying to a pair of tau leptons in proton–proton collisions at $\sqrt{s}$ = 13 TeV with the ATLAS detector*, ATLAS-CONF-2018-021, URL: http://cds.cern.ch/record/2621794.

[8] ATLAS Collaboration, *Evidence for the $H \to b\bar{b}$ decay with the ATLAS detector*, JHEP **12** (2017) 024, arXiv: 1708.03299 [hep-ex].

[9] ATLAS Collaboration, *A search for the rare decay of the Standard Model Higgs boson to dimuons in pp collisions at $\sqrt{s}$ = 13 TeV with the ATLAS Detector*, ATLAS-CONF-2018-026, URL: http://cdsweb.cern.ch/record/2628763.

[10] ATLAS Collaboration, *Search for the Standard Model Higgs boson produced in association with top quarks and decaying into a $b\bar{b}$ pair in pp collisions at $\sqrt{s}$ = 13 TeV with the ATLAS detector*, Phys. Rev. D (2017), arXiv: 1712.08895 [hep-ex].

[11] ATLAS Collaboration, *Evidence for the associated production of the Higgs boson and a top quark pair with the ATLAS detector*, Phys. Rev. D **97** (2018) 072003, arXiv: 1712.08891 [hep-ex].

[12] ATLAS Collaboration, *Observation of Higgs boson production in association with a top quark pair at the LHC with the ATLAS detector*, (2018), arXiv: 1806.00425 [hep-ex].

[13] ATLAS and CMS Collaborations, *Combined Measurement of the Higgs Boson Mass in pp Collisions at $\sqrt{s}$ = 7 and 8 TeV with the ATLAS and CMS Experiments*, Phys. Rev. Lett. **114** (2015) 191803, arXiv: 1503.07589 [hep-ex].

[14] CMS Collaboration, *Measurements of Higgs boson properties in the diphoton decay channel in proton-proton collisions at $\sqrt{s}$ = 13 TeV*, (2018), arXiv: 1804.02716 [hep-ex].

[15] CMS Collaboration, *Measurements of properties of the Higgs boson in the four-lepton final state at $\sqrt{s}$ = 13 TeV*, CMS-PAS-HIG-18-001, 2018, URL: https://cds.cern.ch/record/2621419.

[16] CMS Collaboration, *Measurements of properties of the Higgs boson decaying to a W boson pair in pp collisions at $\sqrt{s}$ = 13 TeV*, (2018), arXiv: 1806.05246 [hep-ex].

[17] CMS Collaboration, *Observation of the Higgs boson decay to a pair of τ leptons*, Phys. Lett. B **779** (2018) 283, arXiv: 1708.00373 [hep-ex].

[18] CMS Collaboration, *Evidence for the Higgs boson decay to a bottom quark–antiquark pair*, Phys. Lett. B **780** (2018) 501, arXiv: 1709.07497 [hep-ex].

[19] CMS Collaboration, *Search for the standard model Higgs boson decaying into two muons in pp collisions at sqrt(s)=13TeV*, CMS-PAS-HIG-17-019, 2017, URL: https://cds.cern.ch/record/2292159.

[20] CMS Collaboration, *Observation of $t\bar{t}H$ production*, Phys. Rev. Lett. **120** (2018) 231801, arXiv: 1804.02610 [hep-ex].

[21] CMS Collaboration, *Combined measurements of the Higgs boson's couplings at $\sqrt{s}$ = 13 TeV*, CMS-PAS-HIG-17-031, 2018, URL: https://cds.cern.ch/record/2308127.

[22] LHC Higgs Cross Section Working Group, S. Heinemeyer et al., *Handbook of LHC Higgs Cross Sections: 3. Higgs Properties*, CERN-2013-004 (2013), arXiv: 1307.1347 [hep-ph].

[23] ATLAS Collaboration, *Constraints on new phenomena via Higgs boson couplings and invisible decays with the ATLAS detector*, JHEP **11** (2015) 206, arXiv: 1509.00672 [hep-ex].

[24] ATLAS Collaboration, *The ATLAS Experiment at the CERN Large Hadron Collider*, JINST **3** (2008) S08003.

[25] ATLAS Collaboration, *ATLAS Insertable B-layer Technical Design Report*, CERN-LHCC-2010-013, ATLAS-TDR-19 (2010), URL: http://cds.cern.ch/record/1291633.

[26] P. Nason, *A new method for combining NLO QCD with shower Monte Carlo algorithms*, JHEP **0411** (2004) 040, arXiv: hep-ph/0409146.

[27] S. Frixione, P. Nason and C. Oleari, *Matching NLO QCD computations with Parton Shower simulations: the POWHEG method*, JHEP **0711** (2007) 070, arXiv: 0709.2092 [hep-ph].

[28] S. Alioli, P. Nason, C. Oleari and E. Re, *A general framework for implementing NLO calculations in shower Monte Carlo programs: the POWHEG BOX*, JHEP **1006** (2010) 043, arXiv: 1002.2581 [hep-ph].

[29] S. Alioli, P. Nason, C. Oleari and E. Re, *NLO Higgs boson production via gluon fusion matched with shower in POWHEG*, JHEP **0904** (2009) 002, arXiv: 0812.0578 [hep-ph].

[30] K. Hamilton, P. Nason, E. Re and G. Zanderighi, *NNLOPS simulation of Higgs boson production*, JHEP **1310** (2013) 222, arXiv: 1309.0017 [hep-ph].

[31] K. Hamilton, P. Nason and G. Zanderighi, *Finite quark-mass effects in the NNLOPS POWHEG+MiNLO Higgs generator*, JHEP **1505** (2015) 140, arXiv: 1501.04637 [hep-ph].

[32] S. Catani and M. Grazzini, *An NNLO subtraction formalism in hadron collisions and its application to Higgs boson production at the LHC*, Phys. Rev. Lett. **98** (2007) 222002, arXiv: hep-ph/0703012.

[33] K. Hamilton, P. Nason, C. Oleari and G. Zanderighi, *Merging H/W/Z + 0 and 1 jet at NLO with no merging scale: a path to parton shower + NNLO matching*, JHEP **1305** (2013) 082, arXiv: 1212.4504 [hep-ph].

[34] LHC Higgs Cross Section Working Group, D. de Florian et al., *Handbook of LHC Higgs Cross Sections: 4. Deciphering the Nature of the Higgs Sector*, (2016), arXiv: 1610.07922 [hep-ph].

[35] C. Anastasiou, C. Duhr, F. Dulat, F. Herzog and B. Mistlberger, *Higgs Boson Gluon-Fusion Production in QCD at Three Loops*, Phys. Rev. Lett. **114** (2015) 212001, arXiv: 1503.06056 [hep-ph].

[36] C. Anastasiou et al., *High precision determination of the gluon fusion Higgs boson cross-section at the LHC*, JHEP **1605** (2016) 058, arXiv: 1602.00695 [hep-ph].

[37] S. Actis, G. Passarino, C. Sturm and S. Uccirati, *NLO electroweak corrections to Higgs boson production at hadron colliders*, Phys. Lett. B **670** (2008) 12, arXiv: 0809.1301 [hep-ph].

[38] C. Anastasiou, R. Boughezal and F. Petriello, *Mixed QCD-electroweak corrections to Higgs boson production in gluon fusion*, JHEP **0904** (2009) 003, arXiv: 0811.3458 [hep-ph].

[39] M. Grazzini and H. Sargsyan, *Heavy-quark mass effects in Higgs boson production at the LHC*, JHEP **1309** (2013) 129, arXiv: 1306.4581 [hep-ph].

[40] P. Nason and C. Oleari, *NLO Higgs boson production via vector-boson fusion matched with shower in POWHEG*, JHEP **1002** (2010) 037, arXiv: 0911.5299 [hep-ph].

[41] M. Ciccolini, A. Denner and S. Dittmaier, *Strong and electroweak corrections to the production of Higgs + 2-jets via weak interactions at the LHC*, Phys. Rev. Lett. **99** (2007) 161803, arXiv: 0707.0381 [hep-ph].

[42] M. Ciccolini, A. Denner and S. Dittmaier, *Electroweak and QCD corrections to Higgs production via vector-boson fusion at the LHC*, Phys. Rev. D **77** (2008) 013002, arXiv: 0710.4749 [hep-ph].

[43] P. Bolzoni, F. Maltoni, S.-O. Moch and M. Zaro, *Higgs production via vector-boson fusion at NNLO in QCD*, Phys. Rev. Lett. **105** (2010) 011801, arXiv: 1003.4451 [hep-ph].

[44] O. Brein, A. Djouadi and R. Harlander, *NNLO QCD corrections to the Higgs-strahlung processes at hadron colliders*, Phys. Lett. B **579** (2004) 149, arXiv: hep-ph/0307206 [hep-ph].

[45] A. Denner, S. Dittmaier, S. Kallweit and A. Muck, *Electroweak corrections to Higgs-strahlung off W/Z bosons at the Tevatron and the LHC with HAWK*, JHEP **1203** (2012) 075, arXiv: 1112.5142 [hep-ph].

[46] L. Altenkamp, S. Dittmaier, R. V. Harlander, H. Rzehak and T. J. E. Zirke, *Gluon-induced Higgs-strahlung at next-to-leading order QCD*, JHEP **1302** (2013) 078, arXiv: 1211.5015 [hep-ph].

[47] J. Alwall, R. Frederix, S. Frixione, V. Hirschi, F. Maltoni et al., *The automated computation of tree-level and next-to-leading order differential cross sections, and their matching to parton shower simulations*, JHEP **1407** (2014) 079, arXiv: 1405.0301 [hep-ph].

[48] W. Beenakker, S. Dittmaier, M. Krämer, B. Plumper, M. Spira et al., *NLO QCD corrections to $t\bar{t}H$ production in hadron collisions*, Nucl. Phys. B **653** (2003) 151, arXiv: hep-ph/0211352 [hep-ph].

[49] S. Dawson, C. Jackson, L. Orr, L. Reina and D. Wackeroth, *Associated Higgs production with top quarks at the large hadron collider: NLO QCD corrections*, Phys. Rev. D **68** (2003) 034022, arXiv: hep-ph/0305087 [hep-ph].

[50] Y. Zhang, W.-G. Ma, R.-Y. Zhang, C. Chen and L. Guo, *QCD NLO and EW NLO corrections to $t\bar{t}H$ production with top quark decays at hadron collider*, Phys. Lett. B **738** (2014) 1, arXiv: 1407.1110 [hep-ph].

[51] S. Frixione, V. Hirschi, D. Pagani, H. S. Shao and M. Zaro, *Weak corrections to Higgs hadroproduction in association with a top-quark pair*, JHEP **1409** (2014) 065, arXiv: 1407.0823 [hep-ph].

[52] M. Wiesemann et al., *Higgs production in association with bottom quarks*, JHEP **02** (2015) 132, arXiv: 1409.5301 [hep-ph].

[53] S. Dawson, C. Jackson, L. Reina and D. Wackeroth, *Exclusive Higgs boson production with bottom quarks at hadron colliders*, Phys. Rev. D **69** (2004) 074027, arXiv: hep-ph/0311067 [hep-ph].

[54] S. Dittmaier, M. Krämer and M. Spira, *Higgs radiation off bottom quarks at the Tevatron and the CERN LHC*, Phys. Rev. D **70** (2004) 074010, arXiv: hep-ph/0309204 [hep-ph].

[55] R. V. Harlander and W. B. Kilgore,
Higgs boson production in bottom quark fusion at next-to-next-to leading order,
Phys. Rev. D **68** (2003) 013001, arXiv: hep-ph/0304035 [hep-ph].

[56] H.-L. Lai, M. Guzzi, J. Huston, Z. Li, P. M. Nadolsky et al.,
New parton distributions for collider physics, Phys. Rev. D **82** (2010) 074024,
arXiv: 1007.2241 [hep-ph].

[57] F. Demartin, F. Maltoni, K. Mawatari and M. Zaro,
Higgs production in association with a single top quark at the LHC, Eur. Phys. J. C **75** (2015) 267,
arXiv: 1504.00611 [hep-ph].

[58] T. Sjöstrand, S. Mrenna and P. Z. Skands, *A Brief Introduction to PYTHIA 8.1*,
Comput. Phys. Commun. **178** (2008) 852, arXiv: 0710.3820 [hep-ph].

[59] S. Gieseke, A. Ribon, M. H. Seymour, P. Stephens and B. Webber,
Herwig++ 1.0: An Event generator for e+ e- annihilation, JHEP **0402** (2004) 005,
arXiv: hep-ph/0311208.

[60] The ATLAS Collaboration, *Measurement of the Z/γ^* boson transverse momentum distribution in pp collisions at $\sqrt{s} = 7$ TeV with the ATLAS detector*, JHEP **09** (2014) 145,
arXiv: 1406.3660 [hep-ex].

[61] S. Agostinelli et al. (GEANT4 Collaboration), *GEANT4: a simulation toolkit*,
Nucl. Instrum. Methods **506** (2003) 250.

[62] J. Allison et al. (GEANT4 Collaboration), *GEANT4 Developments and Applications*,
IEEE Trans. Nucl. Sci. **53** (2006) 270.

[63] ATLAS Collaboration, *The ATLAS Simulation Infrastructure*, Eur. Phys. J. C **70** (2010) 823,
arXiv: 1005.4568 [physics.ins-det].

[64] ATLAS Collaboration, *Measurement of the photon identification efficiencies with the ATLAS detector using LHC Run-1 data*, (2016), arXiv: 1606.01813 [hep-ex].

[65] ATLAS Collaboration, *Electron efficiency measurements with the ATLAS detector using the 2015 LHC proton–proton collision data*, ATLAS-CONF-2016-024, 2016,
URL: https://cds.cern.ch/record/2157687.

[66] ATLAS Collaboration, *Muon reconstruction performance of the ATLAS detector in proton–proton collision data at $\sqrt{s} = 13$ TeV*, Eur. Phys. J. C **76** (2016) 292, arXiv: 1603.05598 [hep-ex].

[67] ATLAS Collaboration, *Jet energy scale measurements and their systematic uncertainties in proton–proton collisions at $\sqrt{s} = 13$ TeV with the ATLAS detector*,
Phys. Rev. D **96** (2017) 072002, arXiv: 1703.09665 [hep-ex].

[68] ATLAS Collaboration,
Measurements of b-jet tagging efficiency with the ATLAS detector using $t\bar{t}$ events at $\sqrt{s} = 13$ TeV,
(2018), arXiv: 1805.01845 [hep-ex].

[69] ATLAS Collaboration, *Performance of missing transverse momentum reconstruction with the ATLAS detector using proton–proton collisions at $\sqrt{s} = 13$ TeV*, (2018),
arXiv: 1802.08168 [hep-ex].

[70] G. Cowan, K. Cranmer, E. Gross and O. Vitells,
Asymptotic formulae for likelihood-based tests of new physics,
Eur. Phys. J. C **71** (2011) 1554, Erratum in Eur. Phys. J. C73 (2013) 2501,
arXiv: 1007.1727 [physics.data-an].

[71] ATLAS Collaboration, *Measurements of the Higgs boson production and decay rates and coupling strengths using pp collision data at $\sqrt{s}$ = 7 and 8 TeV in the ATLAS experiment*, Eur. Phys. J. C **76** (2016) 6, arXiv: 1507.04548 [hep-ex].

[72] ATLAS Collaboration, *Search for the Decay of the Higgs Boson to Charm Quarks with the ATLAS Experiment*, (2018), arXiv: 1802.04329 [hep-ex].

[73] ATLAS Collaboration, *Search for Higgs and Z Boson Decays to $J/\psi\gamma$ and $\Upsilon(n\mathrm{S})\gamma$ with the ATLAS Detector*, Phys. Rev. Lett. **114** (2015) 121801, arXiv: 1501.03276 [hep-ex].

[74] T. Lee, *A Theory of Spontaneous T Violation*, Phys. Rev. D **8** (1973) 1226.

[75] J. F. Gunion and H. E. Haber, *The CP conserving two Higgs doublet model: The Approach to the decoupling limit*, Phys. Rev. D **67** (2003) 075019, arXiv: hep-ph/0207010.

[76] G. Branco et al., *Theory and phenomenology of two-Higgs-doublet models*, Phys. Rept. **516** (2012) 1, arXiv: 1106.0034 [hep-ph].

[77] Y. A. Gol'fand and E. P. Likhtman, *Extension of the Algebra of Poincare Group Generators and Violation of p Invariance*, JETP Lett. **13** (1971) 323, [Pisma Zh.Eksp.Teor.Fiz.13:452-455,1971].

[78] D. V. Volkov and V. P. Akulov, *Is the Neutrino a Goldstone Particle?*, Phys. Lett. **B46** (1973) 109.

[79] J. Wess and B. Zumino, *Supergauge Transformations in Four-Dimensions*, Nucl. Phys. **B70** (1974) 39.

[80] J. Wess and B. Zumino, *Supergauge Invariant Extension of Quantum Electrodynamics*, Nucl. Phys. **B78** (1974) 1.

[81] S. Ferrara and B. Zumino, *Supergauge Invariant Yang-Mills Theories*, Nucl. Phys. **B79** (1974) 413.

[82] A. Salam and J. A. Strathdee, *Supersymmetry and Nonabelian Gauges*, Phys. Lett. **51B** (1974) 353.

[83] S. L. Glashow and S. Weinberg, *Natural Conservation Laws for Neutral Currents*, Phys. Rev. **D15** (1977) 1958.

[84] E. A. Paschos, *Diagonal Neutral Currents*, Phys. Rev. **D15** (1977) 1966.

[85] P. Fayet, *Supergauge Invariant Extension of the Higgs Mechanism and a Model for the electron and Its Neutrino*, Nucl. Phys. **B90** (1975) 104.

[86] P. Fayet, *Supersymmetry and Weak, Electromagnetic and Strong Interactions*, Phys. Lett. **B64** (1976) 159.

[87] P. Fayet, *Spontaneously Broken Supersymmetric Theories of Weak, Electromagnetic and Strong Interactions*, Phys. Lett. **B69** (1977) 489.

[88] L. Maiani, A. D. Polosa and V. Riquer, *Bounds to the Higgs Sector Masses in Minimal Supersymmetry from LHC Data*, Phys. Lett. **B724** (2013) 274, arXiv: 1305.2172 [hep-ph].

[89] A. Djouadi et al., *The post-Higgs MSSM scenario: Habemus MSSM?*, Eur. Phys. J. **C73** (2013) 2650, arXiv: 1307.5205 [hep-ph].

[90] A. Djouadi, L. Maiani, A. Polosa, J. Quevillon and V. Riquer,
Fully covering the MSSM Higgs sector at the LHC, JHEP **06** (2015) 168,
arXiv: 1502.05653 [hep-ph].

Appendix

This appendix includes supplementary figures and tables not included in the body of the note. Table 11 and Figure 15 show the results of a fit to the data using as free parameters the ratios of the branching ratios into $\gamma\gamma$, ZZ^*, WW^*, $\tau\tau$ and $b\bar{b}$ to their values in the SM. The Higgs boson production processes are assumed to follow SM predictions.

Figure 18 shows the same plot as presented in Figure 10, but with in addition a lower inset showing the ratio of the values to their SM expectations.

Figures 16 and 17 show the same combined contours as shown in Figures 4 and 8 respectively, without the contours for the inputs analyses overlaid.

Figures 19, 20, 21 and 22 provide the correlation matrices obtained in fits to data using the models described respectively in Sections 5.4.1, 5.4.2, 5.4.3, 5.4.4 and 5.4.5.

Table 11: Best-fit values and uncertainties of the decay branching ratios of the Higgs boson, measured under SM assumptions for the Higgs boson production processes. The total uncertainties are decomposed into components for data statistics, experimental systematic uncertainties, and theory uncertainties on the modeling of the signal and background processes. SM predictions [34] are shown for the branching ratio into each decay channel. The five-dimensional compatibility with the SM hypothesis corresponds to a p-value of $p_{\mathrm{SM}} = 75.0\%$.

Branching ratio	Value	Uncertainty				
		Total	Stat.	Exp.	Sig. theo.	Bkg. theo.
$\mathrm{B}_{\gamma\gamma}/\mathrm{B}^{\mathrm{SM}}_{\gamma\gamma}$	1.08	$^{+0.13}_{-0.12}$	$\left(\pm 0.08\right.$	$^{+0.08}_{-0.07}$	$^{+0.06}_{-0.05}$	$\left.\pm 0.01\right)$
$\mathrm{B}_{ZZ}/\mathrm{B}^{\mathrm{SM}}_{ZZ}$	1.20	$^{+0.15}_{-0.14}$	$\left(\pm 0.12\right.$	± 0.05	$^{+0.07}_{-0.06}$	$\left.\pm 0.02\right)$
$\mathrm{B}_{WW}/\mathrm{B}^{\mathrm{SM}}_{WW}$	1.14	± 0.17	$\left(\pm 0.10\right.$	± 0.10	$^{+0.07}_{-0.06}$	$\left.^{+0.08}_{-0.07}\right)$
$\mathrm{B}_{\tau\tau}/\mathrm{B}^{\mathrm{SM}}_{\tau\tau}$	1.11	$^{+0.29}_{-0.26}$	$\left(\pm 0.18\right.$	$^{+0.17}_{-0.16}$	$^{+0.13}_{-0.09}$	$\left.^{+0.06}_{-0.05}\right)$
$\mathrm{B}_{bb}/\mathrm{B}^{\mathrm{SM}}_{bb}$	1.07	$^{+0.32}_{-0.30}$	$\left(^{+0.19}_{-0.18}\right.$	± 0.14	$^{+0.12}_{-0.08}$	$\left.^{+0.19}_{-0.18}\right)$

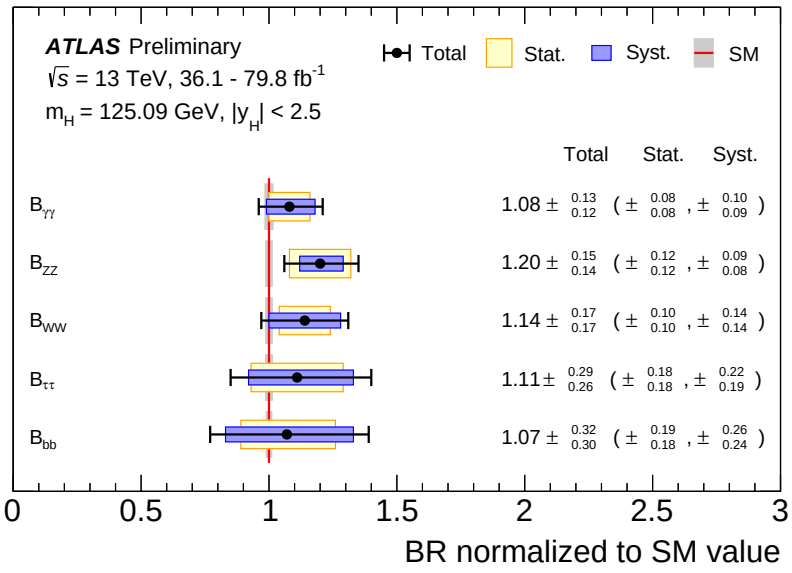

Figure 15: Branching ratios for $H \to \gamma\gamma$, $H \to ZZ^*$, $H \to WW^*$, $H \to \tau\tau$ and $H \to b\bar{b}$ normalized to their SM predictions, measured under SM assumptions for the Higgs boson production processes. The black error bars, blue boxes and yellow boxes show the total, systematic, and statistical uncertainties in the measurements, respectively. The blue bands indicate the theory uncertainties on the predictions.

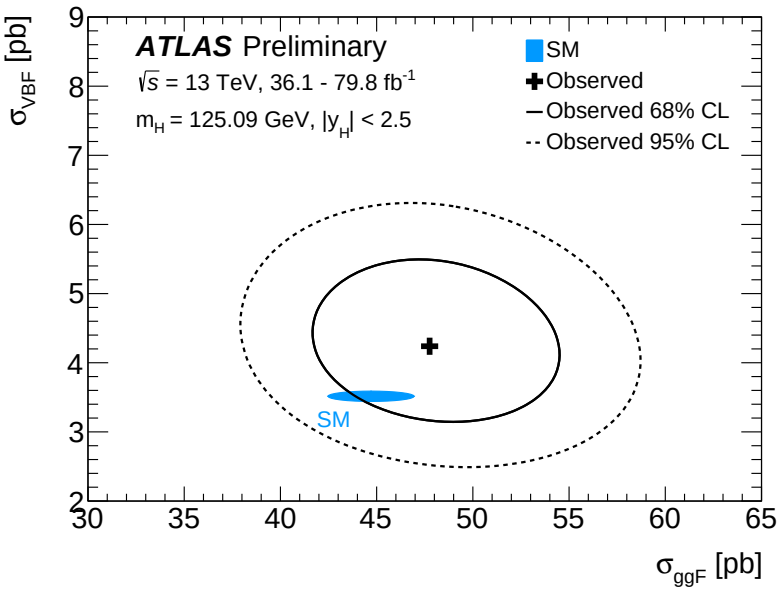

Figure 16: Observed contours at 68% and 95% CL in the plane of σ_{VBF} versus σ_{ggF}, defined in the asymptotic approximation by $-2\log\Lambda = 2.28$ and 5.99, respectively. The cross indicates the best-fit value and the solid ellipse the SM prediction. The Higgs boson decay branching fractions are fixed to their SM values.

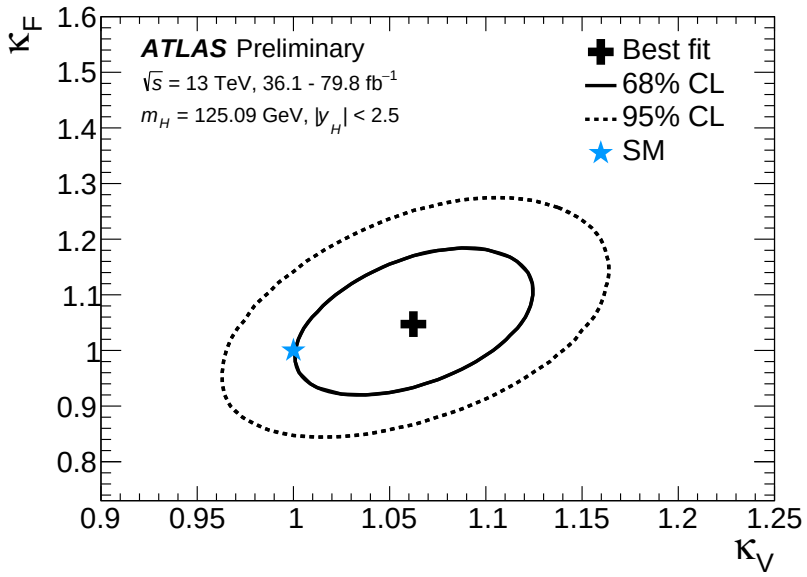

Figure 17: Observed contours at 68% and 95% CL in the (κ_F, κ_V) plane, defined in the asymptotic approximation by $-2\log\Lambda = 2.28$ and 5.99, respectively. The cross indicates the best-fit value and the star the SM prediction.

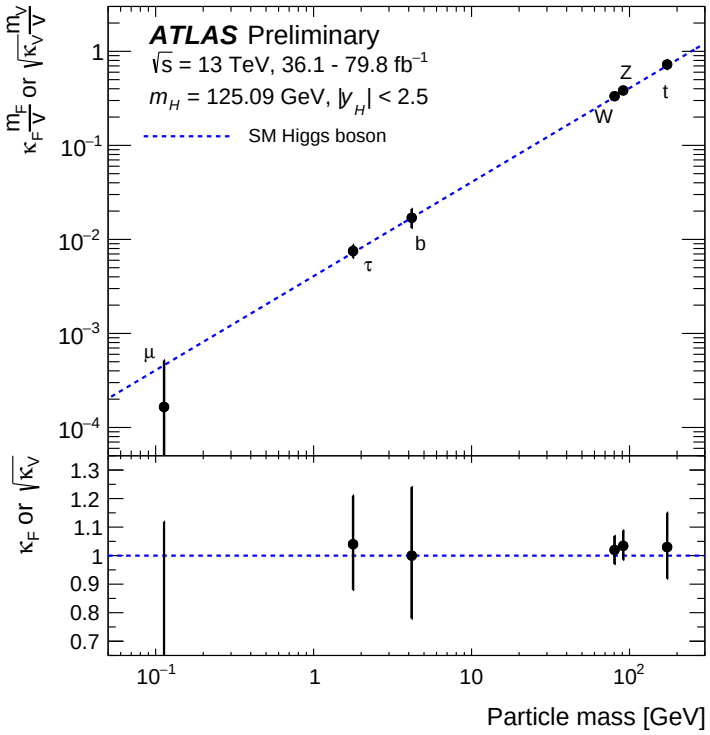

Figure 18: Reduced coupling strength modifiers $\kappa_F \frac{m_F}{v}$ for fermions ($F = t, b, \tau, \mu$) and $\sqrt{\kappa_V}\frac{m_V}{v}$ for weak gauge bosons ($V = W, Z$) as a function of their masses m_F and m_V, respectively, and the vacuum expectation value of the Higgs field $v = 246\,\text{GeV}$. The SM prediction for both cases is also shown (dotted line). The couplings modifiers κ_F and κ_V are measured assuming no BSM contributions to the Higgs boson decays, and the SM structure of loop processes such as ggF, $H \to \gamma\gamma$ and $H \to gg$. The lower inset shows the ratios of the values to their SM predictions.

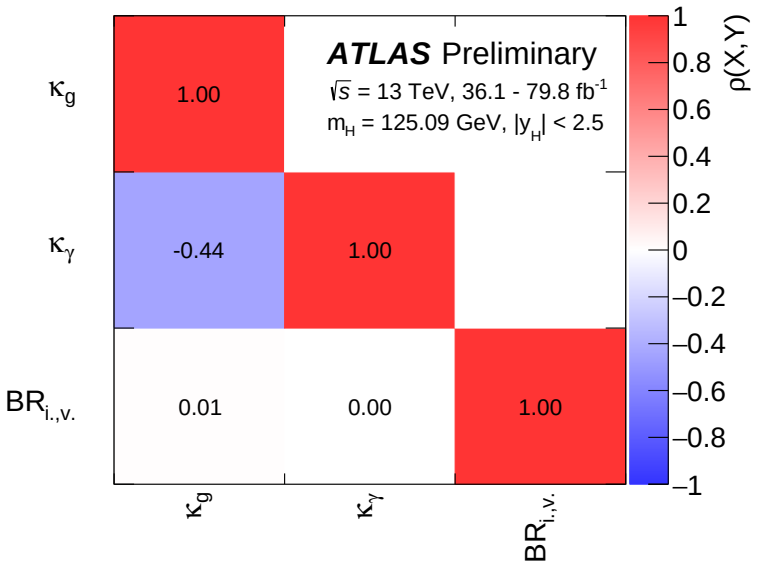

Figure 19: Correlation matrix obtained in the fit to the data of the model described in Section 5.4.2, with B_{BSM} included as a free parameter.

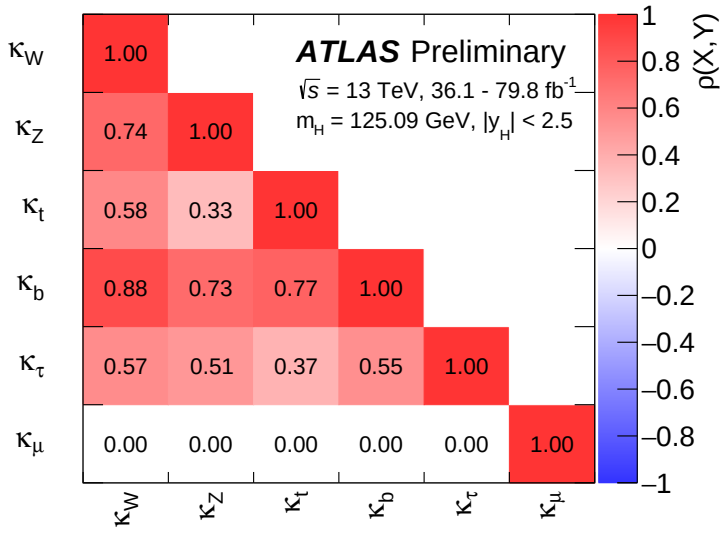

Figure 20: Correlation matrix obtained in the fit to the data of the model described in Section 5.4.3.

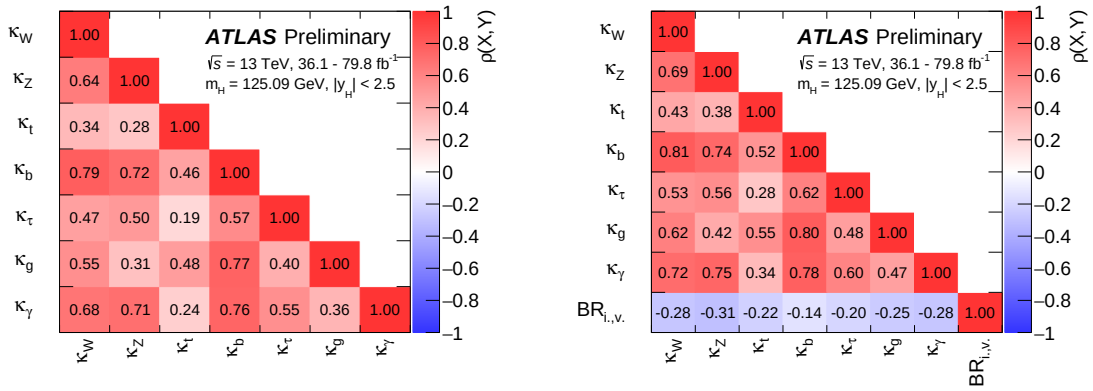

Figure 21: Correlation matrix obtained in the fit to the data of the models described in Section 5.4.4, with B_{BSM} fixed to 0 (left) or included as a free parameter (right).

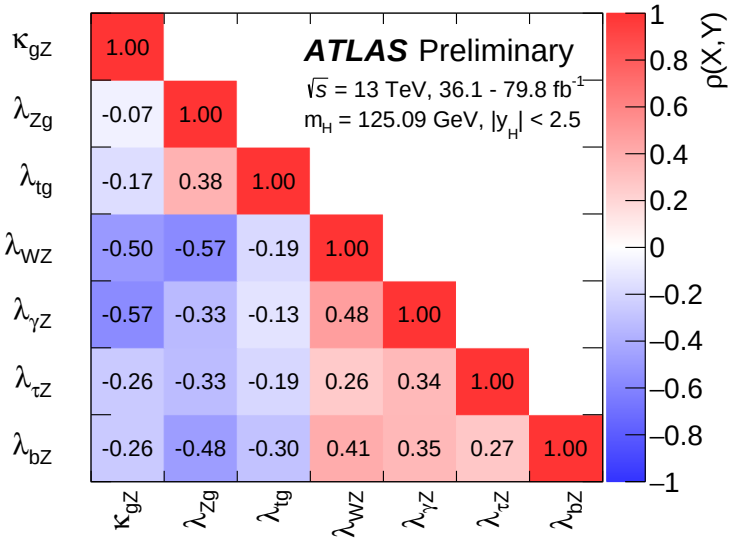

Figure 22: Correlation matrix obtained in the fit to the data of the model described in Section 5.4.5.